3SEB: a remote sensing-based three-source energy balance model to improve global estimations of evapotranspiration in semi-arid tree-grass ecosystems

Vicente Burchard-Levine *(1), Héctor Nieto (2), David Riaño (1,3), William P. Kustas (4), Mirco Migliavacca (5), Tarek S. El-Madany (5), Jacob A. Nelson (5), Ana Andreu (6), Arnaud Carrara (7), Jason Beringer (8), Dennis Baldocchi (9) and M. Pilar Martín (1)*

(1) Environmental Remote Sensing and Spectroscopy Laboratory (SpecLab), Spanish National Research Council (CSIC), Madrid, Spain.
(2) Complutum Tecnologías de la Información Geográfica S.L. (COMPLUTIG), Alcalá de Henares, Spain. Email:
(3) Center for Spatial Technologies and Remote Sensing (CSTARS), John Muir Institute of the Environment, University of California Davis, One Shields Drive, Davis, CA 95616, USA.
(4) U.S. Department of Agriculture, Agriculture Research Service, Hydrology and Remote Sensing Laboratory, Beltsville, MD 20705, USA.
(5) Max Planck Institute for Biogeochemistry, Department Biogeochemical Integration, Hans-Knöll-Str. 10, D-07745 Jena, Germany.
(6) IFAPA - Consejería de Agricultura, Pesca y Desarrollo Rural, Centro Alameda del Obispo, Apdo. 3092, 14080 Cordoba, Spain.
(7) Fundación Centro de Estudios Ambientales del Mediterráneo (CEAM), Valencia 46980, Spain.
(8) School of Geography and Environmental Science, Monash University, Clayton, Victoria, Melbourne, Australia.
(9) Ecosystem Sciences Division, Department of Environmental Science, Policy and Management, 137 Mulford Hall, University of California Berkeley, Berkeley, CA 94720, United States.

***** Correspondence: vicentefelipe.burchard@cchs.csic.es; Tel.: (+34) 916-022-610

Abstract

It is well documented that energy balance and other remote sensing-based evapotranspiration (ET) models face greater uncertainty over water-limited tree-grass ecosystems (TGEs), representing nearly 1/6th of the global land surface. Their dual vegetation strata, the grass dominated understory and tree dominated overstory, make for distinct structural, physiological and phenological characteristics, which challenge models compared to more homogeneous and energy-limited ecosystems. Along with this, the contribution of grasses and trees to total transpiration (T), along with their different climatic drivers, is still largely unknown nor quantified in TGEs. This study proposes a thermal-based three-source energy balance (3SEB) model, accommodating an additional vegetation source within the well-known two-source energy balance (TSEB) model. The model was implemented at both tower and continental scales using eddy-covariance (EC) TGE sites, with variable tree canopy cover and rainfall (P) regimes, and Meteosat Second Generation (MSG) images. 3SEB robustly simulated latent heat (LE) and related energy fluxes in all sites (Tower: LE RMSD ~ 60 W/m^2; MSG: LE RMSD ~ 90 W/m^2), improving over both TSEB and a seasonally changing TSEB (TSEB-2S) models. In addition, 3SEB inherently partitions water fluxes between the tree, grass and soil sources. The modelled T correlated well with EC T estimates ($r > 0.76$), derived from a machine learning ET partitioning method. The T/ET was found positively related to both P and leaf area index, especially compared to the decomposed grass understory T/ET. However, tree and grasses had contrasting relations with respect to monthly P. These results demonstrate the importance in decomposing total ET into the different vegetation sources, as they have distinct climatic drivers, and hence, different relations to seasonal water availability. These promising results improved ET and energy flux estimations over complex TGEs, which may contribute to enhance drought monitoring and understanding, and their responses to climate change feedbacks.

1. Introduction

Climate models project semi-arid tree-grass ecosystems (TGEs), such as savannas, to be disproportionately sensitive to global land and climate change (Bond et al., 2003; Sala et al., 2000). Along with this, long-term water, carbon and energy flux data are notably less available in arid and semi-arid ecosystems compared to humid or mesic systems (Biederman et al., 2017). Remote sensing (RS) and modeling alleviate the relative lack of data however, these are often poorly constrained and/or do not sufficiently represent their more complex heterogeneous features (Whitley et al., 2017). By contrast, global and regional-scale studies highlighted the dominant role that TGEs and other semi-arid ecosystems play on the global biogeochemical cycle, being the main contributor to the trend and inter-annual variability of global carbon and water fluxes (Ahlström et al., 2015; Poulter et al., 2014). These regions are largely water-limited, as opposed to the energy limited, and have unique seasonal and phenological characteristics that are much more coupled to water availability (Baldocchi and Xu, 2007; Higgins et al., 2011). As climate change scenarios predict increases in drought frequency and severity (Sheffield and Wood, 2008; Wang, 2005), an improved understanding of these TGEs is critical to not only better manage their limited hydrological resources, but also due to their important links with the global carbon cycle.

Evapotranspiration (ET), the combination of the abiotically driven surface evaporation and biotic transpiration of vegetation, is an important proxy to determine drought events (e.g., González-Dugo et al., 2021). It is a major flux of the water cycle, often more than 90% of incoming annual precipitation (P) in semi-arid catchments (García et al., 2013), and of the surface energy balance (SEB) as latent heat flux (LE). Eddy-covariance (EC) flux tower networks such as FLUXNET (Baldocchi, 2020; Chu et al., 2017; Running et al., 1999) provide LE observations at numerous sites worldwide. Although the prevalent lack of energy balance closure (e.g., Stoy et al., 2013) is generally attributed, at least partly, to an underestimation of LE (Foken et al., 2011; Leuning et al., 2012). Since EC measurements only offer information over a footprint of several hundred meters, RS is the most feasible source to obtain spatially distributed global and regional ET estimates (Glenn et al., 2007). Among them, SEB models find a good compromise between being physically-based, but without needing extensive data inputs nor parameters to constrain them (Kustas and Anderson, 2009). For this reason, regional and global ET products widely use SEB models (Allen et al., 2015; Anderson et al., 2020; Guzinski et al., 2020; Senay et al., 2013). These models compute ET as the residual of the energy balance, where the available energy (AE), the difference between net radiation (Rn) and ground heat flux (G), is partitioned between sensible heat (H) and LE fluxes. SEB modeling exploits the thermal infrared region (TIR; 8-14 µm) to retrieve the land surface temperature (LST), using it as the main boundary condition to give a proxy on root-zone soil moisture and vegetation status.

There are several types of thermal-based SEB models (e.g., Allen et al., 2007; Bastiaanssen, 2000; Norman et al., 1995; Su, 2002). They largely differ in how they address the difference between the radiometric (LST) and aerodynamic temperature (T_0). ‘Single-source’ models treat the surface as a single composite layer and may use an additional excess resistance term (Lhomme et al., 1997; Verhoef et al., 1997) and/or apply a local calibration procedure that is constrained by end-member pixels (e.g., Allen et al., 2007; Bastiaanssen, 2000). However, these adjustments are often highly parameterized (Boulet et al., 2015), need local calibration (Kustas et al. 2016) or rely on certain assumptions being met at the area of interest. A 'dual-source' approach instead decouples the surface temperature and energy exchange into vegetation and soil components, considering the directional effects of the TIR sensor observation (Anderson et al., 1997; Boulet et al., 2015; Norman et al., 2003, 1995). This more physically based formulation avoids the need for large empirical adjustments, and more adequately represents sparse vegetation cover, common in semi-arid ecosystems. The two-source energy balance (TSEB) model (Kustas and Norman, 1999; Norman et al., 1995) has been robustly applied in diverse landscapes, including for water stressed conditions (e.g., Gonzalez-Dugo et al., 2009; Guzinski et al., 2020; Kustas et al., 2019; Li et al., 2019; Timmermans et al., 2007).

However, ET models show limitations in more structurally complex landscapes, such as TGEs (e.g., Andreu et al., 2018; Burchard-Levine et al., 2020; Cleugh et al., 2007; Majozi et al., 2017; Ramoelo et al., 2014). TGEs represent about 1/6th of the Earth's surface (Sulla-Menashe et al., 2019) and are a prominent land cover within semi-arid regions. Their scattered (or open) tree overstory superimposing a continuous herbaceous understory have very different structural and phenological characteristics. These features, combined with the complex non-linear relationship between model parameters and flux output, causes for greater model uncertainty (Burchard-Levine et al., 2021, 2020). To improve ET simulations through a two-source perspective, Burchard-Levine et al. (2020) proposed a seasonally changing TSEB (TSEB-2S) to accommodate the contrasting phenology of trees and grasses. In a similar Mediterranean TGE, Andreu et al. (2018) calibrated the initial potential transpiration estimate in TSEB and adjusted the wind profile scheme to incorporate the effects of both the overstory and understory on wind turbulence. However, while these adjustments improved the flux estimations in TGEs, they do not directly account for the effect of the dual vegetation layer, limiting their applicability to other TGE sites.

To overcome these limitations, this study proposes a remote sensing based three-source energy balance (3SEB) model, integrating the tree-grass-soil layers present in TGEs within its model structure. The inherent decoupling of fluxes across these layers seeks to improve the understanding of transpiration (T) and plant water use efficiency, along with their relation to water availability and climate change. This also provides a framework to quantify the different tree and grass contribution to T, with currently very little available knowledge in this respect, especially at the ecosystem scale. EC measurements benchmarked 3SEB at four TGE sites located in Australia, Spain (2) and USA. The natural gradient between sites including large variability in tree cover (19 to 48%), climate (annual rainfall (P): 300 to 850 mm/y) and physiology (evergreen vs deciduous trees) required examining the T/ET relation with P and the leaf area index (LAI). In addition, TSEB (Norman et al., 1995) and TSEB-2S (Burchard-Levine et al., 2020) simulations were evaluated against 3SEB. Furthermore, as a proof-of-concept, 3SEB was implemented at quasi-global scale using data from the Spinning Enhanced Visible and Infrared Imager (SEVIRI) onboard Meteosat Second Generation (MSG) satellites. The model outputs were produced for TGE pixels within the MSG extent (~Africa, Europe and parts of Asia and South America) and evaluated over three EC sites in Spain, Senegal and South Africa.

2. Methods

2.1 Three-source energy balance (3SEB) model structure

The 3SEB model structure is based on the TSEB (Norman et al., 1995) surface resistance and energy balance equations. 3SEB adds a vegetation layer to the TSEB model scheme to account for the dual vegetation layers. The original TSEB formulation presented both the ‘series’ and ‘parallel’ formulations to describe the soil-vegetation-atmosphere interactions (Norman et al., 1995). The ‘parallel’ approach portrays no interaction between the soil/substrate and vegetation components, with both components interacting directly with the atmosphere. By contrast, the ‘series’ formulation assumes interaction between the two sources with both contributing to the temperature in the canopy air space (i.e., aerodynamic temperature) (Kustas and Norman, 1999b). The ‘parallel’ model should not be confused with the ‘patch’ model as described in Lhomme et al. (2012), where the surface is portrayed as ‘patches’ of vegetation and soil/substrate that are fully uncoupled and act independently of each other (Kustas and Norman, 1999b; Lhomme et al., 2012). Within the ‘parallel’ resistance framework, the vegetation source still has an influence on the wind speed attenuation below the canopy, and the radiation transmitting through canopy towards the soil surface (Kustas and Norman, 1999b). A combined ‘parallel-series’ three-source modeling approach is proposed here (Fig. 1).

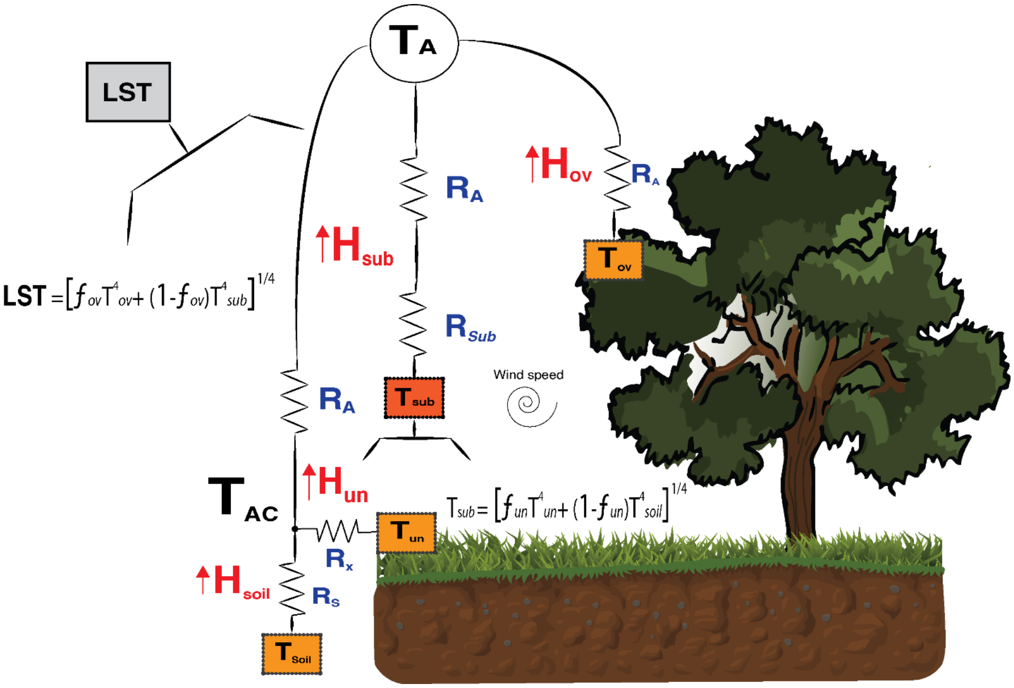

Figure 1. The three-source energy balance (3SEB) model scheme.

Assuming blackbody emissivity, LST is partitioned between soil (T_{soil}), understory (T_{un}) and overstory vegetation (T_{ov}) temperatures as follows:

$$LST = \left[f_{(\theta),ov}T_{ov}^4 + \left(1 - f_{(\theta),ov}\right)T_{sub}^4\right]^{1/4} \tag{1.1}$$

$$T_{sub} = \left[f_{(\theta),un} T_{un}^4 + \left(1 - f_{(\theta),un}\right) T_{soil}^4\right]^{1/4} \tag{1.2}$$

where T_{sub} is the understory vegetation + soil substrate (sub) temperature (K); $f_{(\theta),c}$ is the fraction of vegetation (c for either understory, un, or overstory, ov) observed by the sensor and estimated as: $f_{(\theta),c} = 1 - exp(-k_{bc}\Omega_c F_c)$, where F is the local LAI (m^2/m^2), Ω is the clumping index (-), and k_b is the beam extinction coefficient described in Campbell and Norman (1998). Section S2 in supplementary material (SI) describes Ω and k_b estimations. Using this approach, the energy balance is decoupled between the three sources:

$$LE_{ov} = Rn_{ov} - H_{ov} \tag{2.1}$$

$$LE_{un} = Rn_{un} - H_{un} \tag{2.2}$$

$$LE_{soil} = Rn_{soil} - H_{soil} - G \tag{2.3}$$

where LE is latent heat flux (W m^{-2}) and G is the soil heat flux (W m^{-2}). Using the layer approach (Lhomme et al. 2012), the fluxes of each source sum up to obtain the total bulk surface flux (i.e., $Fl = Fl_{ov} + Fl_{un} + Fl_{soil}$, where Fl represents the energy fluxes, either Rn, LE or H). The radiative transfer model (RTM) described in Chapter 15 of Campbell and Norman (1998), which was slightly adapted to consider multiple vegetation layers (see section S2 in SI), simulated the radiation transmission through the canopies. G is estimated through the approach of Santanello and Friedl (2003). To solve the system of equations, a two-step approach is applied. Firstly, the surface is treated as a parallel (i.e., uncoupled) tree-substrate system to obtain H_{ov} and H_{sub} using the heat transport equation (Eq. 3.1, 3.2):

$$H_{ov} = \frac{\rho C_p (T_{ov} - T_A)}{R_A} \tag{3.1}$$

$$H_{sub} = \frac{\rho C_p (T_{sub} - T_A)}{R_A + R_{sub}} \tag{3.2}$$

where ρC_p is the volumetric heat capacity of air (J m^{-3} K^{-1}); R_A is the aerodynamic resistance to heat transfer based on the Monin-Obukhov similarity theory (Eq. S9 in SI) and R_{Sub} is the resistance to heat transfer in the surface boundary layer above substrate layer (s m^{-1}) (Eq. S10 in SI). Subsequently, H_{un} and H_{soil} are estimated through a series (i.e., coupled) approach (Eq. 4.1, 4.2, 4.3).

$$H_{un} = \frac{\rho C_p (T_{un} - T_{AC})}{R_X} \tag{4.1}$$

$$H_{soil} = \frac{\rho C_p (T_{soil} - T_{AC})}{R_S} \tag{4.2}$$

$$H_{sub} = H_{un} + H_{soil} = \frac{\rho C_p (T_{AC} - T_A)}{R_A} \tag{4.3}$$

where T_{AC} is the air temperature in the canopy space (K) and is equivalent to the aerodynamic temperature; R_X is the bulk canopy resistance to heat transfer (s m^{-1}; Eq. S11) and R_S is the resistance to heat transfer in the boundary layer above soil layer (s m^{-1}; Eq. S10). Eq. 3.2 is inverted to estimate T_{sub}, which serves as the boundary condition to derive T_{un} and T_{soil} in Eq. 1.2. The three-source resistance scheme in Fig. 1 is based on the resistance formulation described in Appendix B of Norman et al. (1995).

Since T_{ov}, T_{un} and T_{soil} are unknown *a priori*, the Priestley-Taylor (PT) formulation, as in Norman et al. (1995), computes a first estimate of the canopy LE and H for both overstory and understory using:

$$LE_c = \alpha_{PT} f_g \left(\frac{\Delta}{\Delta + \gamma}\right) Rn_c \tag{5.1}$$

$$H_c = Rn_c - LE_c = Rn_c \left[1 - \alpha_{PT} f_{g,c} \left(\frac{\Delta}{\Delta + \gamma}\right)\right] \tag{5.2}$$

where LE_c is the initial canopy transpiration estimate (W m^{-2}); α_{PT} is the PT coefficient (default is 1.26) (-), defined in this case only for the vegetation canopy component (Agam et al., 2010; Kustas and Anderson, 2009); $f_{g,c}$ is the green vegetation fraction and hence actively transpiring (-); Δ is the slope of the saturation vapor pressure curve (kPa K^{-1}) at air temperature (T_A); and γ is the psychrometric constant (kPa K^{-1}). The subscript *c* here refers to the understory or overstory vegetation component.

The PT formulation initializes the model to solve the system of equations. However, this assumes the canopy is transpiring at a potential rate (without water stress). While the vegetation canopy behaves more conservatively compared to the bulk surface (Agam et al., 2010), if the plant is stressed, the PT equation overestimates LE at the canopy level, underestimating the canopy temperature. This induces an overestimation of soil and substrate temperatures and, thus, $H_{sub/soil}$ to conserve the total surface temperature (Eq. 1.1-1.2). As such, to preserve the energy balance (Eq. 2.1-2.3), this would produce a negative soil or substrate LE (i.e., condensation), which is considered unrealistic for daytime conditions. Therefore, an iteration procedure reduces α_{PT} to mimic water stress until there is conservation in the radiometric and energy balance under feasible bounds (i.e., non-negative daytime component LE). 3SEB implements this procedure separately for the overstory-substrate and the understory-soil systems, since it is expected that each vegetation layer experiences water stress differently, both in terms of magnitude and timing. As such, the understory-soil layer applies the PT formulation considering T_{sub} as the main boundary condition (Eq. 1.2 and 3.2). The overstory-substrate uses LST as the main boundary condition (Eq. 1.1 and 3.1). Refer to the model source code for further details (https://github.com/VicenteBurchard/3SEB).

A combination of proximal and satellite RS data forced the 3SEB model. All sites collected half-hourly proximal TIR measurements. This approach is more efficient than daily or bi-weekly satellite near-noon overpasses, since the later does not capture the entire temporal and seasonal dimension and requires clear-sky conditions. However, the model implementation would essentially be the same using spatially discrete LST imagery (see section 2.4). LAI is another important variable that dictates the radiation transmission between the various layers (Campbell and Norman, 1998; section S1 in SI). It also characterizes the roughness and aerodynamic resistance of the surface (Norman et al., 1995; section S2 in SI). In this study, Moderate Resolution Imaging Spectroradiometer (MODIS) onboard the Terra and Aqua satellite platforms retrieved LAI and f_g, key for the initial transpiration estimate (Eq. 5.1, 5.2). Section 2.3 describes details on LST, LAI and f_g retrievals. In addition, the respective sites collected meteorological data to characterize the turbulent and atmospheric condition (section 2.2). Other auxiliary inputs included the vegetation structure (height, cover and leaf width) (section 2.4) and parameters related to the resistance and radiation transfer sub-models (section S1 and S2 in SI).

2.2 Study sites

Four experimental TGE EC sites across three continents evaluated the 3SEB model: Majadas de Tiétar (ES-LM1) and Albuera (ES-Abr) in Spain, the Tonzi Ranch in California, USA (US-Ton) and Dry River in Australia (AU-Dry) (Fig. 2). At all sites, P is mostly concentrated during specific wet seasons and suffer a sustained seasonal drought period. The wet season largely falls during autumn (~October-November) and spring (~March-April), except for AU-Dry (~December-February). Sites vary in P and LAI (Fig. 3), from the relatively arid ES-Abr (P ~300 mm/year) with large seasonal range in LAI (~0.4-2 m^2/m^2) to the more humid AU-Dry (P ~850 mm/year), with comparatively less range in LAI (~0.8-1.8 m^2/m^2). The peak biomass period occurs in ~April-May, but slightly earlier for AU-Dry in ~February-March (Fig. 3). The dry season occurs for all sites roughly in ~June-August, when most of the understory herbaceous species largely senesce.

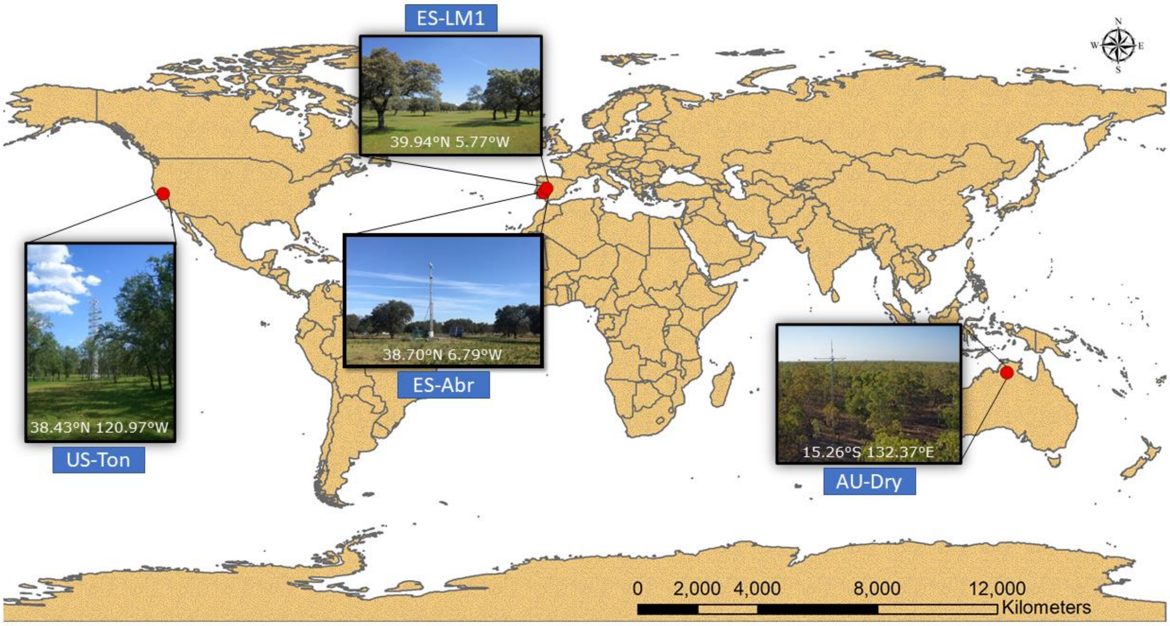

Figure 2. TGE EC locations that implemented and evaluated 3SEB at the site scale

Distinct tree overstory and grass understory compose all TGE sites with variable vegetation composition and density. ES-LM1 is a managed agro-forested area in central Spain, known as *dehesa* (El-Madany et al., 2018), where evergreen Holm Oak (*Quercus ilex*. L.) represents roughly 20% of the surface and stands at a mean height of 8.7 m (Bogdanovich et al., 2021; El-Madany et al., 2020). At ~200 km south, ES-Abr is a more arid *dehesa* also composed of Holm Oaks, but with slightly larger tree fractional cover (24%) and lower canopy height (6.6m) (El-Madany et al., 2020). Deciduous Blue Oaks (*Quercus douglasii* H. & A) dominate the overstory with a larger 48% cover at the US-Ton site, an oak savanna woodland located on the lower foothills of the Sierra Nevada Mountains in California, USA (Baldocchi et al., 2010). Evergreen eucalyptus species (*Eucalyptus tetrodonta* F.Muell, *Eucalyptus terminalis* F.Muell and *Eucalyptus dichromophloia* F.Muell*)* standing at 12.3 m mean height dominate in AU-Dry, with roughly 25% cover (Hutley et al., 2011; Sea et al., 2011).

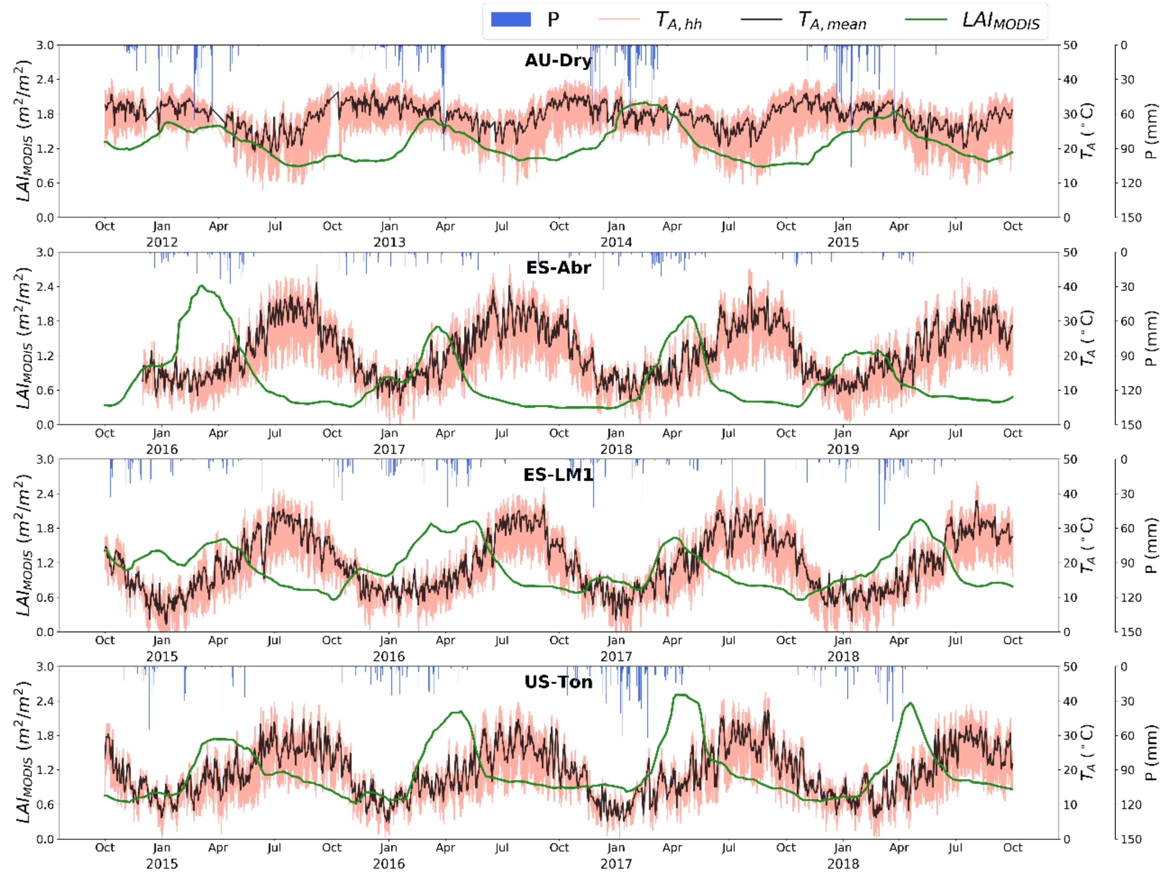

Figure 3. Rainfall (P), half-hourly air temperature ($T_{A,hh}$), daytime mean temperature ($T_{A,mean}$) and leaf area index (LAI) time series during the simulation period for AU-Dry, ES-Abr, ES-LM1 and US-Ton.

All four EC sites have similar instrumentation to force and evaluate 3SEB, including three-dimensional sonic anemometer (Gill LTD[1], Lymington, UK), along with infrared gas analyzers

---

[1] The use of trade, firm, or corporation names in this article is for the information and convenience of the reader. Such use does not constitute official endorsement or approval by the US Department of Agriculture or the Agricultural Research Service of any product or service to the exclusion of others that may be suitable

(Li-Cor Inc., Lincoln, NE, USA) and four-component net radiometers (CNR4, Kipp and Zonen, Delft, Netherlands). Refer to the respective reference of each site for more details (Table S1). Half-hourly meteorological and flux data were downloaded for the four-year simulation period shown in Fig 3 and listed in Table S1, using hydrological years (1-Oct to 30-Sept) to fully capture the main wet and growing seasons. These include incoming shortwave (SW_{in}) and longwave (LW_{in}) irradiance, outgoing longwave irradiance (LW_{out}), T_A, relative humidity (RH), and wind speed (u). Additionally, *in-situ* energy balance observations of Rn, LE, H and G benchmarked the model performance. Allocating residuals to the observed LE ensured the energy balance closure (i.e., $\sum[LE + H] \,/\, \sum[R_N - G]$), which ranged from 0.76 and 0.83 across sites, with the assumption that errors in LE are larger than H (e.g., Foken et al., 2011), as applied in similar studies (e.g., Burchard-Levine et al., 2020; Guzinski et al., 2014; Kustas et al., 2012).

In addition to these four sites, two other EC sites were also used to benchmark the 3SEB model when applied at the continental scale (see section 2.3.3). These were the Dhara site in Senegal (SN-Dhr; Tagesson et al., 2013; 2015) and the Skukuza site in South Africa (ZA-Kru; Archibald et al., 2009; Scholes, 2013). Datasets were collected from FLUXNET2015 release (Pastorello et al., 2020).

2.3 The 3SEB model implementation and evaluation

2.3.1 Model set-up

Each site implemented 3SEB at the half-hourly time step for a four-year period (Table S1). LST and meteorological forcing (i.e., SW_{in}, T_A, u, RH) were incorporated at this time step, while vegetation biophysical variables (i.e., LAI, f_g) were forced daily (see section S4.2 of SI).

LST was estimated from LW radiation measurements from CNR4 (Kipp & Zonen, Delft, Netherlands) radiometers (see section S4.1 in SI). The MODIS LAI v006 (MCD15A3H) product provided green LAI (LAI_{green}) at 500 m spatial resolution (LAI_{MODIS}). Because the non-green or non-photosynthetically active vegetation (i.e. dead leaves/plants or wooded material) influence the aerodynamic and radiative transfer, total LAI (LAI_{total}) or plant area index (PAI) would be more appropriate but it is not available globally. The Gutman and Ignatov (1998) approach based on the normalized difference vegetation index (NDVI) estimated f_g. NDVI time series at the pixel centered over each site for the simulation period came from the MODIS daily Nadir BRDF-adjusted Reflectance v006 (MCD43A4) product. Pacheco-Labrador et al. (2017) demonstrated the 500×500 m pixel to adequately represent the EC flux footprint area. 3SEB must distinguish total LAI and f_g for each vegetation layer; their decomposition into each vegetation sources and other processing details are given in section S4.2 of the SI.

EC measurements benchmarked 3SEB flux outputs (H, LE, Rn and G) at both half-hourly and daily scales. Additionally, 3SEB ET partitioning (T/ET) was evaluated against the Transpiration Estimation Algorithm (TEA) (Nelson et al., 2018). TEA is a data-driven method, which uses the carbon (i.e., gross primary production, GPP) and water (i.e., ET) relations to decouple the T signal from ET. For more details on the TEA algorithm, see Nelson et al. (2020, 2018). ES-LM1 and US-Ton also had EC tower measurements below the tree overstory to further evaluate the modelled flux partitioning.

TSEB (Norman et al., 1995) and TSEB-2S (Burchard-Levine et al., 2020) simulations were additionally performed for comparison purpose. Since TSEB has only one vegetation source assumed in the model structure, effective input and parameter values depict the mixed surface (Table 2). TSEB-2S adjusts the parameterization of the vegetation source depending on the assumed dominant vegetation source, a grass dominated (understory-soil system) growing phase and a tree-dominated (overstory-soil) drought phase. For more information on TSEB-2S, refer to Burchard-Levine et al. (2020).

Table 1 lists the structural vegetation parameters implemented in 3SEB and TSEB. TSEB-2S applies the 'understory' or 'overstory' configuration depending on the phenological phase (section S5 in SI). To clarify, f_c is different to $f_{(\theta),ov}$ and $f_{(\theta),un}$ from Eq. 1.1 and 1.2. The f_c mostly characterizes the distribution and canopy clumping (Eq. S4.1), while $f_{(\theta),ov}$ and $f_{(\theta),un}$, functions of LAI and sensor viewing angle, are the vegetation fraction viewed by the sensor and partitions the temperature contribution from the different sources. For example, the understory f_c (i.e., $f_{c,un}$) is maintained constant at 1 throughout the simulation period, since the understory rather homogeneously covers the entire soil surface, even during the dry period (Table 1). Nevertheless, f_g quantifies the vegetation percentage that is photosynthetically active and, by contrast, varies seasonally (Fig. S1).

Table 1. Structural parameters for the overstory (ov) and understory (un) vegetation for the different EC sites

		3SEB								TSEB			
	Vegetation Parameters	**AU-Dry**		**ES-Abr**		**ES-LM1**		**US-Ton**		**AU-Dry**	**ES-Abr**	**ES-LM1**	**US-Ton**
		ov	**un**	**ov**	**un**	**ov**	**un**	**ov**	**un**	**effective vegetation**	**effective vegetation**	**effective vegetation**	**effective vegetation**
f_c	Fractional cover (-)	0.25	1	0.24	1	0.2	1	0.48	1	1	1	1	1
h_c	Canopy height (m)	12.3	0.5	6.6	0.5	8.7	0.5	9.4	0.5	12.3*	6.6*	8.7*	9.4*
l_w	Effective leaf width (m)	0.05	0.01	0.05	0.01	0.05	0.01	0.05	0.01	0.05	0.05	0.05	0.05
LAI	Leaf area index (m^2/m^2)	LAI$_{\mathrm{ov}}$	LAI$_{\mathrm{un}}$	LAI$_{\mathrm{ov}}$	LAI$_{\mathrm{un}}$	LAI$_{\mathrm{ov}}$	LAI$_{\mathrm{un}}$	LAI$_{\mathrm{ov}}$	LAI$_{\mathrm{un}}$	LAI$_{\mathrm{MODIS}}$	LAI$_{\mathrm{MODIS}}$	LAI$_{\mathrm{MODIS}}$	LAI$_{\mathrm{MODIS}}$
f_g	Green fraction (-)	$f_{g,ov}$	$f_{g,un}$	$f_{g,ov}$	$f_{g,un}$	$f_{g,ov}$	$f_{g,un}$	$f_{g,ov}$	$f_{g,un}$	$f_{g,total}$	$f_{g,total}$	$f_{g,total}$	$f_{g,total}$

** See section S7 in SI*

2.3.2 Model performance evaluation

In-situ LAI measurements evaluated the MODIS-based understory (LAI$_{\mathrm{un}}$) and overstory (LAI$_{\mathrm{ov}}$) LAI decomposition, as required by 3SEB. These data were only available for ES-LM1 and US-Ton. In ES-LM1, the retrieved LAI$_{\mathrm{un}}$ were benchmarked against measured understory LAI from 24 field campaigns between 2014-10-31 and 2018-07-16 through the FLUXPEC (http://www.lineas.cchs.csic.es/fluxpec/) and SynerTGE (http://www.lineas.cchs.csic.es/synertge/) projects. In this site, destructive sampling with the separation of green/non-green material and leaf scanning obtained *in-situ* LAI. The mean of ~20-30 samples acquired during each campaign represented the ecosystem LAI_{un}. Details on field protocols for ES-LM1 are available in Melendo-Vega et al. (2018) and Mendiguren et al. (2015). For US-Ton, *in-situ* LAI_{un} was collected from the Biological, Ancillary, Disturbance, and Metadata (BADM) dataset available through AMERIFLUX. A Li-cor (LI-3100C) area meter (https://www.licor.com/env/products/leaf_area/LI-3100C/) from 400 cm^2 sampling areas measured LAI (Baldocchi and Ma, 2013). *In-situ* LAI_{un} measurements in US-Ton acquired on 33 dates from 2010-02-10 to 2013-05-08 were outside the simulation period, but nonetheless served to benchmark the retrieved LAI_{un}.

The root-mean-square-deviation (RMSD), mean bias (bias), the Nash-Sutcliffe efficiency index (NSE) and the Pearson´s correlation coefficient (r) quantified the modeling performance. In addition, mean daily error plots inspected the seasonal trends of model uncertainty. The standard deviation (σ) of mean daily errors quantified the intra-annual variability, while the mean range of errors for each day of year evaluated the inter-annual variability (IAV).

The estimated T/ET, including separating the understory (T_{un}) and overstory (T_{ov}) transpiration, were related to monthly and annual P. In addition, the Wei et al. (2017) empirical equation (Eq. 9), which evaluated the relation between T/ET and LAI, contextualized the retrieved relationship between photosynthetic activity and T (Wang et al., 2014).

$$\frac{T}{ET} = aLAI^b \tag{9}$$

where a and b correspond to the coefficients optimized for different land classes, which for the ‘grasslands and shrubs’ land classification, including savannas, are 0.69 and 0.28, respectively.

2.3.3 Continental-scale implementation of 3SEB with Meteosat Second Generation data

In addition to site-level model runs, satellite data primarily from the Spinning Enhanced Visible and Infrared Imager (SEVIRI) onboard Meteosat Second Generation (MSG) satellites forced 3SEB. The MSG disk covers Africa, Europe and parts of South America and Asia (Fig. S4 in SI). This area represents roughly 60% of worldwide TGEs (Sulla-Menashe et al., 2019). LST, vegetation indices and shortwave irradiance were acquired from the Land Surface Analysis Satellite Application Facilities (LSA SAF) (https://landsaf.ipma.pt/en/data/catalogue/). The canopy height was obtained from spaceborne LiDAR through the Global Ecosystem Dynamics Investigation (GEDI) L3 product (Dubayah et al., 2021). The Copernicus Global Land Operations (CGLOPS-1) 100m land cover and forest cover product (Tsendbazar et al., 2021) delineated TGE pixels and offered an overstory f_c estimate. Global meteorological data were collected from the Copernicus ECMWF ERA5 reanalysis dataset (Hersbach et al., 2020) and processed similarly to the Sentinels for Evapotranspiration (Sen-ET, Guzinski et al., 2020) approach. Refer to section S8 in the SI for further details on the data sources and processing used to implement 3SEB over the MSG disk.

Model runs were forced at the hourly time step between 9:00 and 18:00 UTC for 2012 over all pixels (pixel size: 0.05°) classified as TGEs within the MSG disk (see section S8.2 in SI). *In-situ* data from ES-LM1, SN-Dhr and ZA-Kru benchmarked this continental approach. Other sites used in this study were not included in this evaluation due to being outside the MSG extent (AU-Dry and US-Ton) or due to data unavailability during the processing period (ES-Abr).

3. Results

3.1 Vegetation biophysical inputs

In ES-LM1, the MODIS-derived LAI_{un} correlated well with both *in-situ* LAI_{total} ($r = 0.71$) and LAI_{green} ($r = 0.83$) (Fig. 4). However, moderate errors were observed, notably compared against LAI_{total} ($RMSD = 0.59$ m^2/m^2). LAI_{un} was systematically lower compared to LAI_{total} ($bias = -0.45$ m^2/m^2), notably during the March-May 2016 peak biomass (Fig. 4b). Nevertheless, LAI_{un} was generally aligned with LAI_{green} ($RMSE = 0.32$ m^2/m^2 and $bias = -0.08$ m^2/m^2). In ES-LM1, as field sampling protocols separated green and non-green material, the $f_{g,un}$ was also assessed (Fig. 4a). The retrieved $f_{g,un}$ aligned reasonably well with *in-situ* measurements in ES-LM1, being well correlated ($r = 0.6$) and capturing the magnitudes ($bias = -0.05$ m^2/m^2). Despite this, modeled $f_{g,un}$ had moderate errors ($RMSE = 0.22$) and a quicker dry down compared to observed values, which sustained peak values for longer (Fig. 4a). In US-Ton, the retrieved LAI_{un} were within similar magnitudes to the observed understory LAI (Fig. 4d). However, correlation was lower ($r = 0.44$), while errors similar ($RMSE = 0.43$ m^2/m^2) as found in ES-LM1.

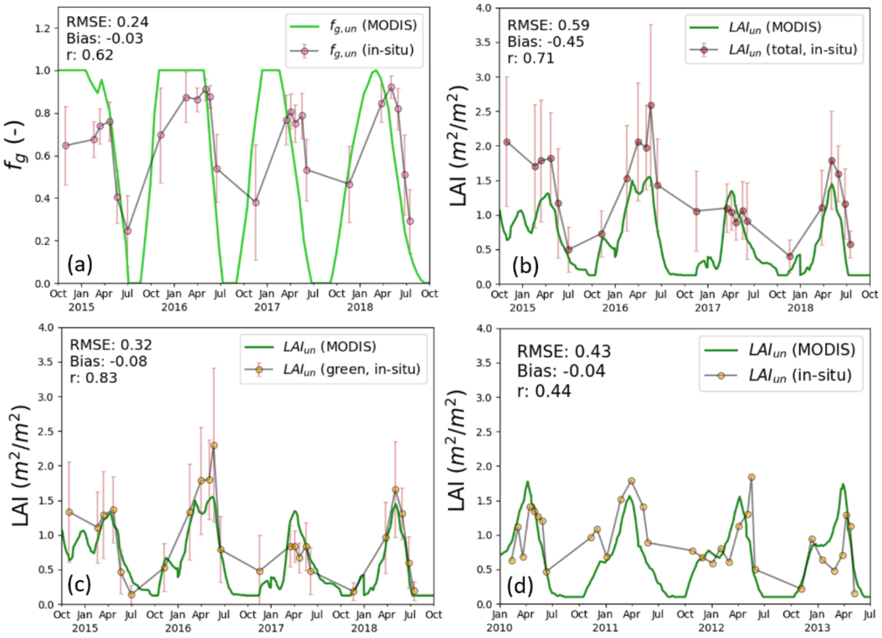

Figure 4. Evaluation of MODIS derived understory green fraction ($f_{g,un}$, *a*) and leaf area index (LAI_{un}) against *in-situ* total (LAI_{total}, b) and green LAI (LAI_{green}, c) measurements in ES-LM1 and US-Ton (d). Red error bars represent the standard deviation of sample values during each field campaign.

3.2 Tower-based flux estimations with 3SEB

For all sites, midday half-hourly LE_{3SEB} correlated well with observed LE (LE_{obs}), with r ranging from 0.81-0.88 (Fig. S3). LE_{3SEB} RMSD ranged between 59 and 67 W/m^2. Errors and bias were generally larger in ES-Abr and US-Ton due to the slight underestimation of H (bias = -38 and -36 W/m^2, respectively). By contrast, H_{3SEB} was slightly overestimated in AU-Dry (bias = 26 W/m^2). For all sites, the NSE was greater than 0.5, which indicated a satisfactory model fit compared to observed data (Moriasi et al., 2007).

The ET_{3SEB} RMSD ranged between 0.35 and 0.48 mm/day (Fig. 5). At the daily scale, the NSE was greater for all sites, ranging from 0.82 to 0.89. In AU-Dry, 3SEB tended to underestimate ET during the Jan-April peak biomass period. By contrast, ES-Abr, ES-LM1 and US-Ton often overestimated ET during the seasonal drought period. For ES-Abr and ES-LM1, this is particularly apparent during the 2016 dry period, largely due to the sustained H underestimation. It is noteworthy that 2016 was an extraordinarily productive year so the LAI_{total}, including non-green elements, was unusually high during the summer (Fig. 4b).

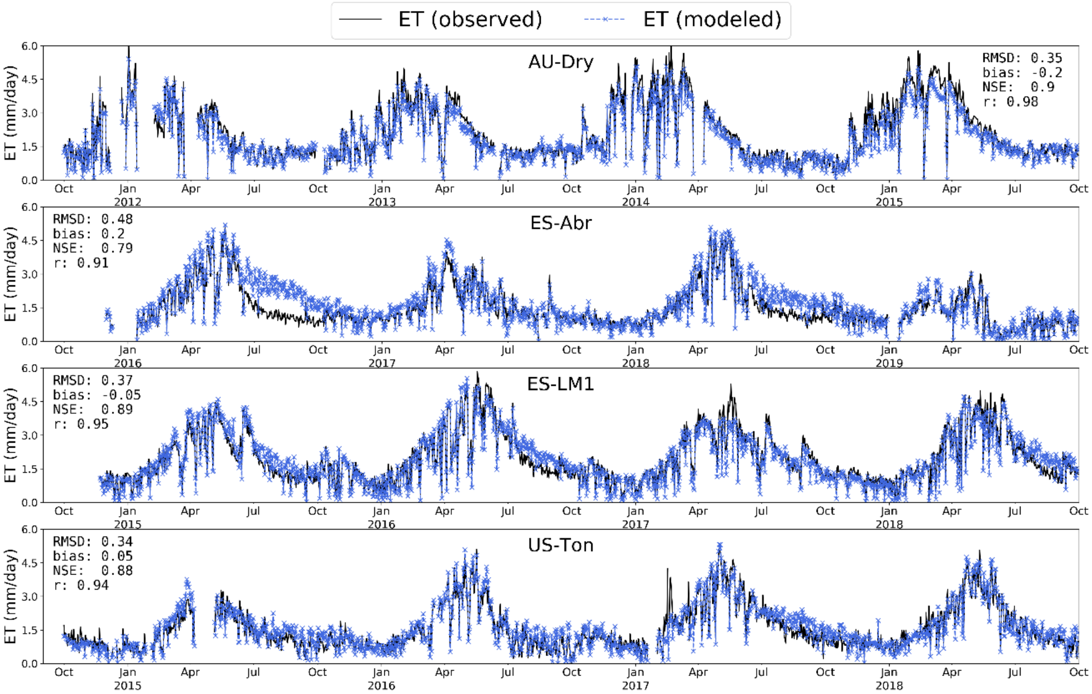

Figure 5. Daily time series of ET_{3SEB} (blue) and observed ET (black) throughout the simulation period.

3.3 Comparison with TSEB and TSEB-2S

TSEB, TSEB-2S and 3SEB model performance indicators (see Table S2) show that midday H_{3SEB} RMSD decreased for all sites from 89 to 66 W/m^2 compared to H_{TSEB}. The H NSE also increased from 0.33 to 0.65. LE_{3SEB} similarly improved for all model evaluation indicators.

Along with overall decrease in bias, 3SEB had less seasonal variability in errors compared to TSEB and TSEB-2S (Fig. 6). For example, in AU-Dry, estimated H with TSEB and TSEB-2S deviated most from observations during the peak growing period (Feb-March), reaching H deviations up to ~200 W/m^2. In ES-Abr, ES-LM1 and US-Ton, H errors with both two-source models were largest during the dry-down and seasonal drought. By contrast, the error distribution of 3SEB remained relatively consistent throughout the year, with σ lower compared to TSEB and TSEB-2S (Fig. 6). This was particularly evident during the seasonal dry-down period in US-Ton and ES-LM1, where TSEB-2S errors tended to increase largely compared to 3SEB (Fig S4). However, TSEB-2S performed similarly to 3SEB in ES-Abr and even had slightly less bias during the peak seasonal drought (~August). The IAV was lowest for 3SEB (~45 W/m^2) and largest for TSEB-2S (~60 W/m^2).

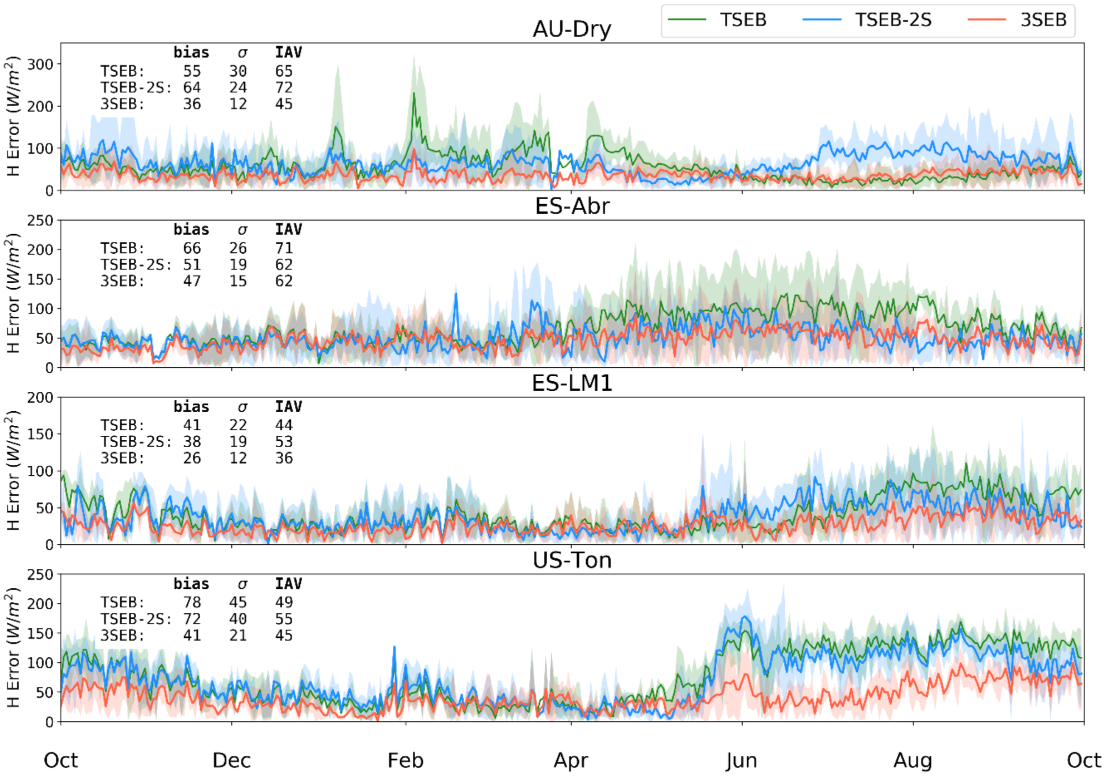

Figure 6. Annual time series of the average daily H errors $(|H_{obs} - H_{mod}|)$ for TSEB (green), TSEB-2S (blue), and 3SEB (red). Shaded area corresponds to the minimum and maximum daily error of the four years assessed. The average H bias, annual standard deviation (σ) and average daily range of error (IAV) are also shown.

3.4 Flux partitioning between ecosystem sources

3.4.1 Flux partition evaluation

The daily T_{3SEB} correlated well with the data-driven T_{TEA} at all sites (Fig. 7; $r > 0.76$). Using the T_{TEA} as the benchmark, errors are also relatively low (RMSD = 0.46 to 0.91 mm/day) and without large systemic biases from 3SEB (bias = -0.03 to 0.6 mm/day). The largest deviations occurred in US-Ton, mostly due to T overestimations during low LAI periods.

In addition, sub-canopy EC towers, available in ES-LM1 and US-Ton, assessed the modeled fluxes from the understory substrate (understory T + soil E). H, instead of LE, benchmarked the partitioning to limit issues related to energy balance (EB) closure and uncertainties with the AE below the overstory canopy. The modeled H_{sub} were highly correlated with those measured for both sites, with r of 0.84 and 0.92 (Fig. 8). However, US-Ton had important systematic biases with an RMSD and bias of 117 and 87 W/m^2, respectively. By contrast, modeled H_{sub} in ES-LM1 had less errors (RMSD: 63 W/m^2) and only slightly overestimated.

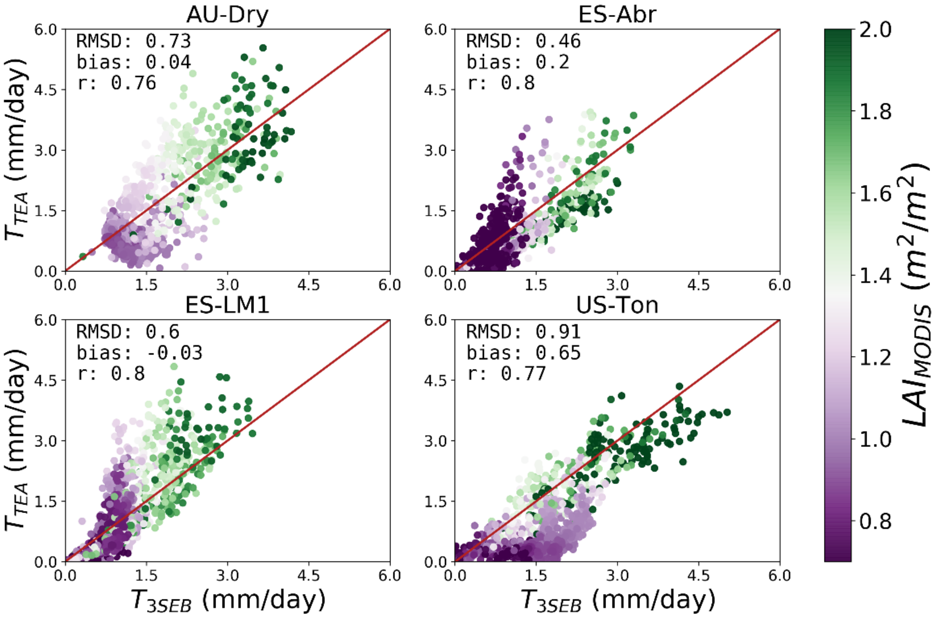

Figure 7. Scatter plots of modelled daily transpiration (T_{3SEB}) versus the TEA estimates (T_{TEA}). Colors visualize the daily ecosystem LAI (LAI_{MODIS}).

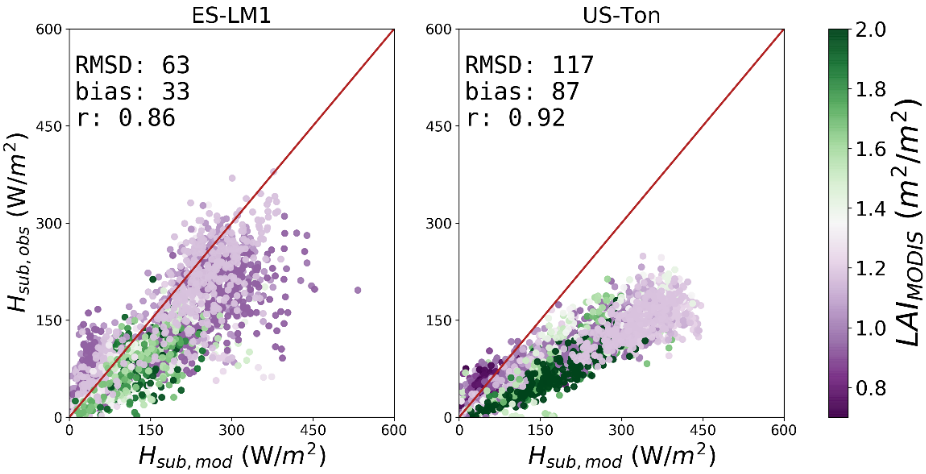

Figure 8. Scatter plots of modelled midday (between 11 and 13 UTC) substrate (understory + soil) H ($H_{sub, mod}$) versus those observed ($H_{sub, obs}$) from the sub-canopy towers in ES-LM1 (left) and US-Ton (right). Colors visualize the daily ecosystem LAI (LAI_{MODIS}).

3.4.2 Seasonal flux partition

The overall mean annual T/ET for all sites was between 46-66%. However, these TGEs are highly seasonal with the phenology of dual vegetation layers inducing large variability to the different contributions to ET (Fig. 9). T_{ov}/ET was largest in AU-Dry (i.e., 45±11 %) and lowest in

ES-Abr and ES-LM1 with mean annual contributions of 31±9 and 34±11 %, respectively. In US-Ton, the mean T_{ov}/ET was much more variable (40±29 %) due to the deciduous nature of the tree species. In ES-Abr and ES-LM1, E_{soil}/ET was generally higher with mean annual contribution of 54±9 and 53±12 %, respectively. The T_{un}/ET in US-Ton had the largest variability (22±20 %), with contribution ranging from nearly 60% during the peak biomass period to ~0% during the seasonal drought.

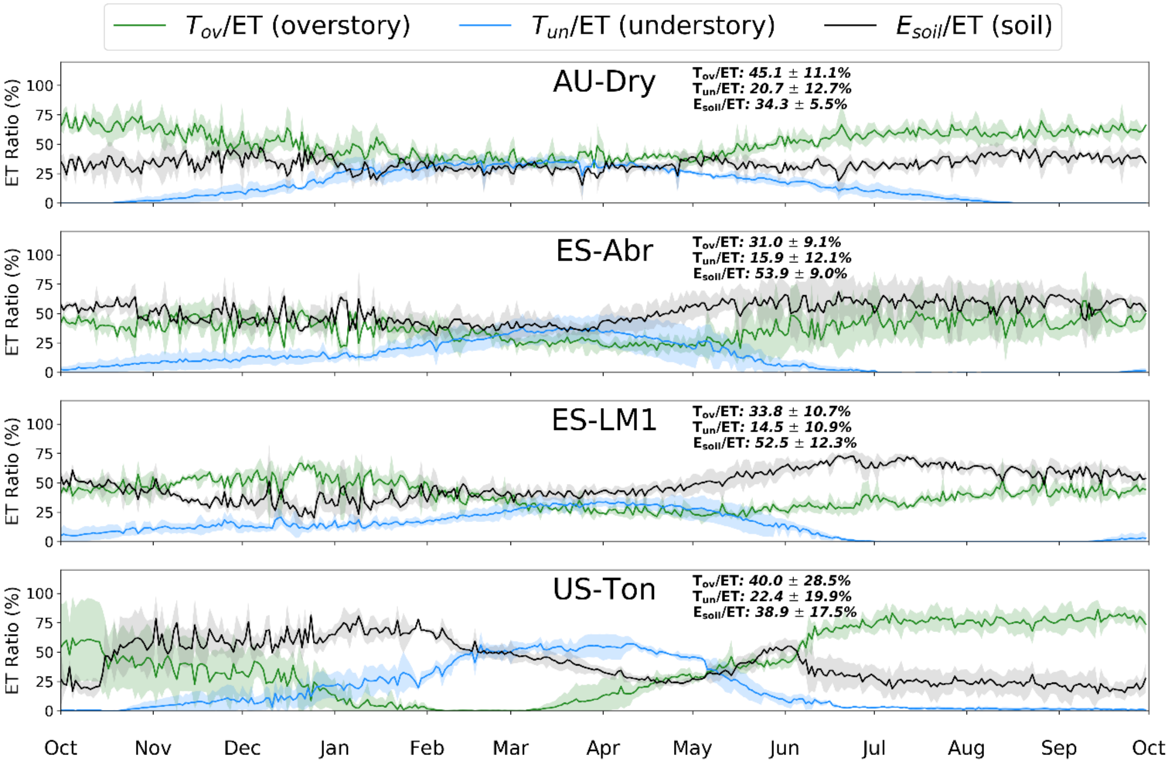

Figure 9. Average daily seasonal ET partitioning into overstory (green), understory (blue) and soil (black) sources as a percentage of total surface ET. Shaded area represents the IAV (i.e., range for that day of year) of the four simulated years.

3.4.3 ET partitioning relation with P and LAI

The results show that T_{ov}/ET and T_{un}/ET have contrasting relations with monthly P (Fig. 10), with the former negatively correlated (r = -0.32, $p < 0.01$), while latter being positively related (r = 0.34, $p < 0.01$). However, at the annual scale, both T_{ov}/ET and T_{un}/ET are positively correlated with P, but the relation with T_{ov}/ET is not as significant (i.e., $p = 0.1$). T/ET showed no trend with monthly P (r = 0.05, $p = 0.51$), but had a significant positive relation with annual P (r = 0.58, $p = 0.02$).

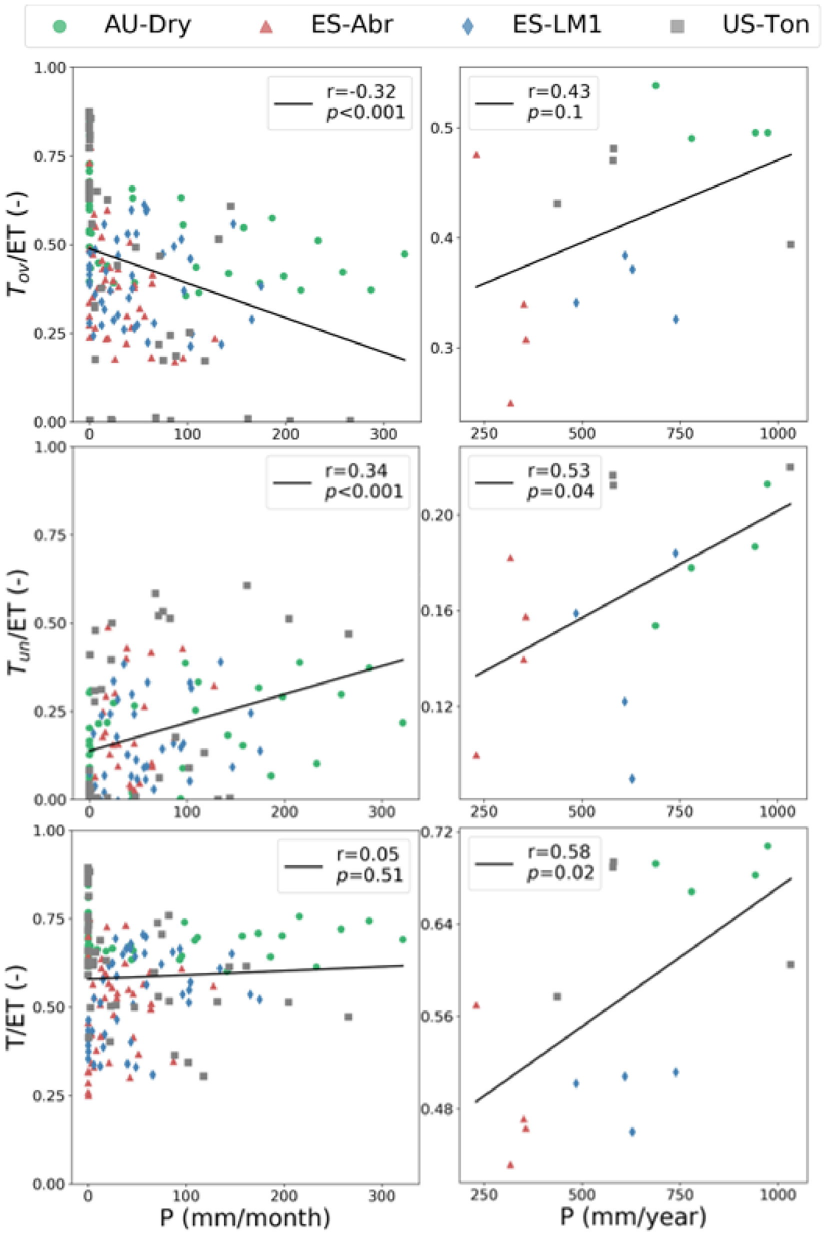

Figure 10. Scatter plots of P versus T_{ov}/ET (upper rows), T_{un}/ ET (center rows) and T/ET (lower rows) at both monthly (left column) and annual (right column) scales.

The empirical Wei et al. (2017) T/ET and LAI regression (Wei2017) was developed using mean site level LAI and T/ET measurements from numerous sites, aggregating over large temporal periods, and not at the monthly time step such as presented here with the 3SEB partitioning (Fig. 11). At the ecosystem level, T/ET is less correlated with LAI (r ~ 0.4). Nevertheless, the relation becomes much stronger and linear when only the ratio transpired from the understory (i.e., T_{un}/ET) is assessed (r = 0.75). Although the fitted regression was linear, the power function of Wei2017 still explained a large portion of the variance (r = 0.71), even though notable biases were observed (RMSD: 0.54). Interestingly, by examining only the substrate system, the ET partitioning

(T_{un}/[T_{un}+E_{soil}]) was very much linked to LAI_{un} (r = 0.86). Additionally, the fitted power trend is more notable and like Wei2017, although T/ET increases more slowly as LAI increases.

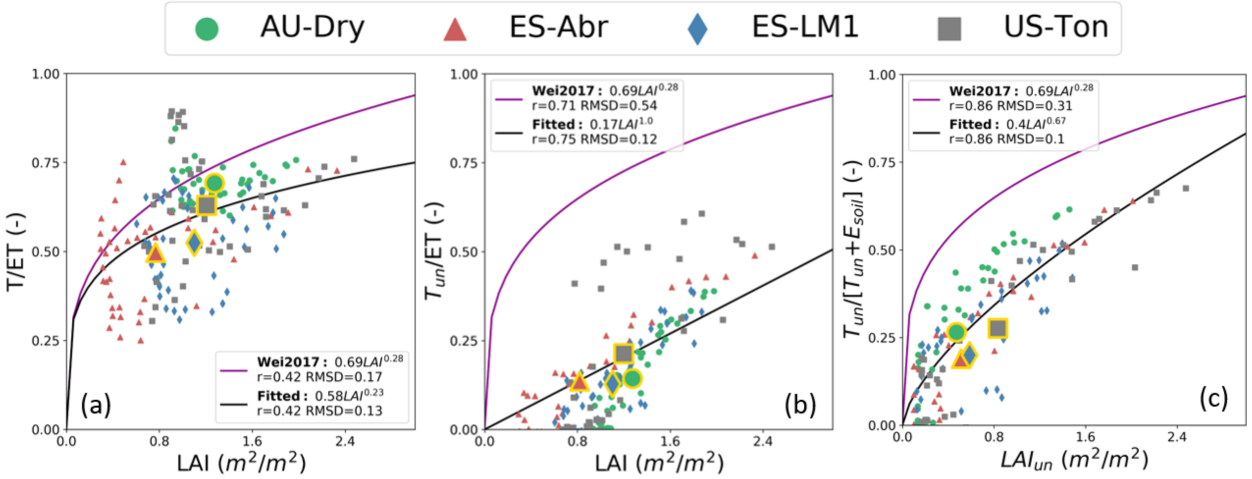

Figure 11. Relationship between monthly LAI and T/ET (a) and T_{un}/ET (b); and LAI_{un} and T_{un}/T_{un}+E_{soil} (c). Black lines are the fitted regression optimizing *a* and *b* coefficients of Eq. 9 and purple lines are the associated relation derived from Wei et al. (2017) with the mean site level averages (yellow).

3.4 Continental 3SEB flux estimations

Fig. 12 shows the estimated 2012 mean annual LE, including the different component partitioning ratios, when 3SEB was forced with at the continental scale using SEVIRI/MSG data. The mean annual T/ET ratio was 50.5% over the entire MSG extent.

Three EC sites (shown in Fig. 12) evaluated the flux outputs from this satellite implementation of 3SEB (Fig. 13). The SEVIRI/MSG 3SEB implementation observed higher errors compared to site-scaled simulations (section 3.2). However, H retrievals, especially for ES-LM1 and SN-Dhr, maintained within similar error magnitudes. Midday hourly H RMSD ranged from 64 to 97 W/m^2 over the three sites, with both ES-LM1 and SN-Dhr observing high correlation with measured fluxes (r > 0.75). ZA-Kru observed higher H errors (RMSD = 97 W/m^2 and r = 0.36). The increases in error were more pronounced for LE, with RMSD and r ranging from 83 to 104 W/m^2 and 0.4 to 0.87, respectively.

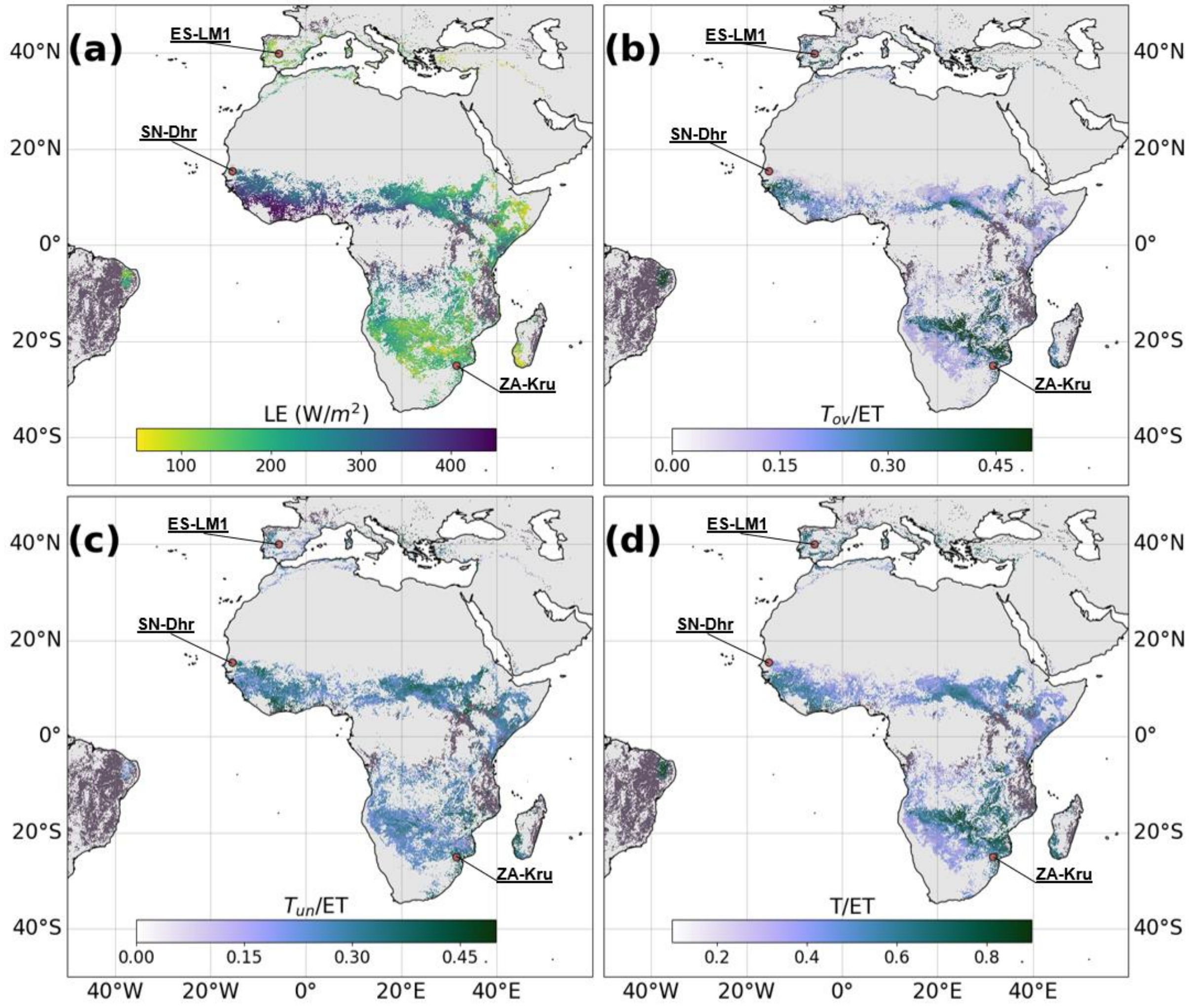

Figure 12. Map of SEVIRI/MSG forced 3SEB estimations of 2012 mean annual LE (a), T_{ov}/ET (b), T_{un}/ET (c) and T/LE (d). Dark grey areas correspond to TGE pixels not processed due to cloud or other processing issues. *In-situ* EC sites are located by red points.

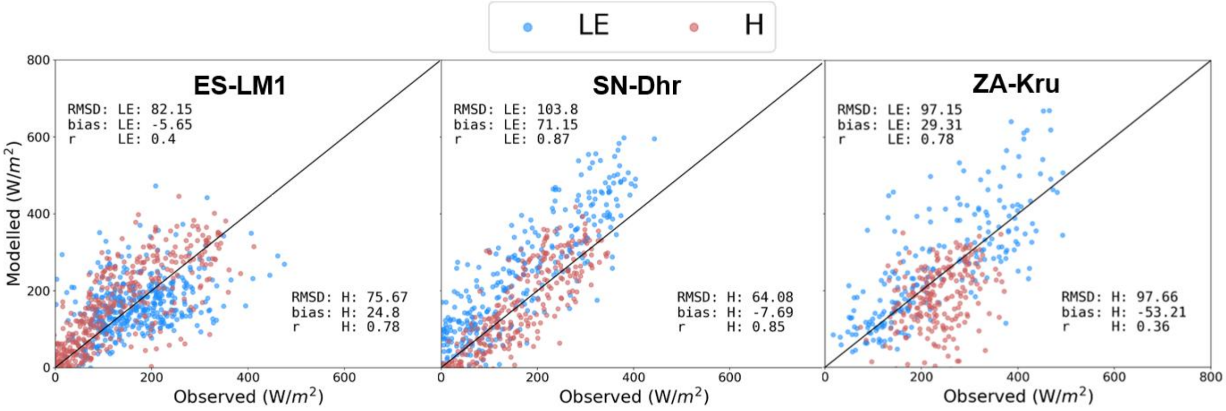

Figure 13. Evaluation of SEVIRI/MSG 3SEB daytime fluxes against tower measurements in 2012 from ES-LM1, SN-Dhr and ZA-Kru

4. Discussion

The proposed 3SEB model improved the depiction and simulation of water and energy fluxes for heterogeneous semi-arid TGE landscapes, typically poorly represented by state-of-the-art models (Majozi et al. 2017; Ramoelo et al. 2014; Whitley et al. 2017). In the four sites, 3SEB accurately simulated ET (RMSD < 0.5 mm/day) and related energy fluxes (midday H RMSD ~60 W/m^2). The model structure also demonstrated robustness when applied at the continental scale (LE RMSD ~90 W/m^2), along with reproducing flux dynamics for sites with spatial and temporal variability in canopy cover, P and LAI. Furthermore, it consistently improved over TSEB and TSEB-2S with fewer overall errors (Table S2), along with less intra- and IAV of errors (Fig. 6). These semi-arid ecosystems often switch from being carbon sinks and sources. Therefore, better capturing the IAV is particularly relevant (Biederman et al., 2017; El-Madany et al., 2020).

As shown in Burchard-Levine et al. (2021), the combination of tree and grass features in TGEs caused large uncertainties when using effective input/parameter values at coarser spatial scales (pixel size > 10 m). Along with spatial complexities, the 3SEB model incorporated the distinct overstory and understory phenological dynamics of the TGEs semi-arid vegetation. Whitley et al. (2017) highlighted these considerations as important characteristics generally not accounted for within land surface models, misrepresenting and generating uncertainty over TGEs. In particular, the seasonal dry-down induces an even greater landscape heterogeneity with important mixing of senesced and active understory vegetation along with the overstory. As shown in Fig. 6 and Fig. S4, 3SEB better captured these transitional periods, as the LAI is decoupled and the phenology of each vegetation source can change independently. It is more challenging to represent the heterogeneity present through effective values (e.g., TSEB) for a landscape with dual vegetation layers (Burchard-Levine et al. 2020, 2021). To account for this, TSEB-2S alters the model parameterization assuming either the understory or overstory vegetation as dominant. However, the sharp change in the parameterization caused uncertainty during the seasonal transition periods, when both vegetation sources co-dominate (Fig. 6; S4). This was particularly evident in US-Ton, where TSEB-2S had large errors at the beginning of the summer season (~June, Fig. 6), subsequently decreasing during the peak seasonal drought periods (~July-August), when the understory had largely senesced.

As a proof of concept, 3SEB was applied at the continental scale over Africa, Europe and neighboring regions from other continents. Quasi-global datasets available from LSA-SAF and ancillary data sources parameterized the model. The promising evaluation over three sites rendered errors only slightly greater than the site-level simulations (Fig. 13). LE errors increased more significantly than H due to more uncertainty in the AE estimation (i.e. Rn – G, see Fig. S9). This was expected due to numerous reasons. First off, the ERA-5 reanalysis meteorological and LSA-SAF shortwave irradiance data inputs are likely to add more uncertainty, compared to locally measured meteorological and irradiance data. Crucially, shortwave irradiance directly affects Rn estimations and, thus, LE as it estimated as the residual of the EB. Fig. S9 shows that LSA-SAF irradiance inputs are highly correlated to tower measurements in all sites. Nevertheless, important errors are present (RSMD >100W/m^2), translating to nosier modeled outputs. Secondly, there is a large spatial scale mismatch between the pixel size (~5km) and the EC tower footprint (~hundreds of meters). This substantially increases pixel heterogeneity, which may induce greater uncertainty to the primary (i.e. LST, LAI) and ancillary (i.e., f_g, f_c, h_c,) inputs (Chu et al., 2021). Despite these greater sources of errors from model inputs, 3SEB performed relatively well at the MSG pixel level, obtaining similar errors statistics as the 20m Sen-ET retrievals (LE RMSD ~80-100 W/m^2; Guzinski et al. 2020), and performed better than the LSA-SAF ET product (see Fig. S8). These promising results demonstrate 3SEB's potential application on the operational level or incorporated within global Earth System Models.

In addition to improving flux estimates in these complex landscapes, 3SEB explicitly decomposes ET into the different vegetation and land surface components. Research on ET partitioning from biotic and abiotic sources (i.e., T/ET) has gained traction because of its key links to plant water use and limitations in the context of climate and agronomic sciences (Anderson et al., 2017; Fisher et al., 2017). Despite current efforts (Ma et al., 2020; Nelson et al., 2020; Stoy et al., 2019), determining T remains a challenge due to its complex relations with soil moisture, climatology, vegetation cover and phenological cues (Perez-Priego et al., 2018; Scott and Biederman, 2017; Wei et al., 2017). Numerous studies indicate that global mean T/ET is roughly 60% (Fatichi and Pappas, 2017; Li et al., 2019; Schlesinger and Jasechko, 2014; Stoy et al., 2019; Wei et al., 2017; Good et al., 2015; Lian et al., 2018; Sun et al., 2019). However, these reported global T/ET values carry large uncertainty, ranging between ~30-90% (Stoy et al., 2019). 3SEB reported here a T/ET between 44-66% at site scale, which aligned well with the TEA algorithm (RMSD: ~ 0.6 mm/day), and 50.5% for the continental-scale (~Africa and Europe) 3SEB simulations (Fig.12d). A meta-analysis of T/ET estimates over 38 semi-arid sites (Sun et al., 2019) reported the T/ET was roughly 50%, as similarly reported in this study.

Soil evaporation (E_{soil}/ET) was largest in ES-Abr and ES-LM1 representing around ~55% of ET. This is in line with Perez-Priego et al. (2017, 2018) who show that the understory ET dominated in ES-LM1. In fact, E_{soil}/ET in Perez-Priego et al. (2018) reached up to ~70% during the growing period through lysimeter measurements and a novel ET partitioning method, similar to that achieved with 3SEB (Fig. 9). The summer drought maintained relatively large E_{soil}/ET. Perez-Priego et al. (2018) observed considerable soil evaporation rates even when the shallow (i.e., sandy) soil was dry, indicating the evaporation rates may be upheld from moisture of the deeper soil (e.g., clay) layer.

While past studies suggested T/ET to be independent from P (e.g., Fatichi and Pappas, 2017; Schlesinger and Jasechko, 2014, Sun et al. 2019), mean annual T/ET correlated positively here with annual P ($r = 0.58$, $p = 0.02$; Fig. 10). In water-limited ecosystems, ET partitioning might be more strongly linked to P and water availability (e.g., Perez-Priego et al., 2018). El-Madany et al. (2020) reported very strong linear correlations between annual P and GPP for ES-Abr and ES-LM1, which has mechanistic links to T. At the monthly scale, T_{un}/ET and T_{ov}/ET had opposing relations with seasonal P. This further demonstrated the contrasting survival strategies of both vegetation functional types. The tree overstory has large root systems to access deeper soil moisture sources and remain physiologically active during the dry season (Archibald and Scholes, 2007; Higgins et al., 2011; Luo et al., 2018). Their growth is less dependent on rainfall events or other meteorological cues (Archibald and Scholes, 2007; Higgins et al., 2011). By contrast, herbaceous understory species respond quickly to water availability, opting for an annual phenology to avoid the drought season (Bond, 2008; Moore et al., 2016). Therefore, T_{ov}/ET is usually greater during the dry months with the inactivity of understory species, and hence the negative correlation. Interestingly, T_{ov}/ET was positively related to P at the annual scale ($r = 0.43$, $p = 0.1$). This fact suggests that, while seasonal water availability is not important for tree species, the long-term P is. However, this non-significant relationship ($p > 0.05$) needs more observations to confirm this trend. At the ecosystem level, there was no significant correlation between monthly T/ET and P ($r = 0.05$, $p = 0.5$), due to the contrasting relation each of the vegetation layers had with seasonal P.

Other studies reported stronger links between T/ET and LAI compared to P (e.g., Sun et al. 2019; Wang et al., 2014; Wei et al., 2017). Wei et al. (2017) developed empirical models for different land cover types to obtain T/ET estimates from LAI. Nevertheless, they stated that savanna ecosystems presented large uncertainties due to the overstory and understory differences in water uptake processes. Indeed, LAI did not explain a large portion of the T/ET variance ($r = 0.4$). However, the relationship was much stronger with LAI ($r = 0.77$), after separating the fluxes to consider only T_{un}/ET. Furthermore, $T_{un}/[T_{un}+E_{soil}]$ was highly correlated with the understory LAI_{un} ($r = 0.83$), with a similar fitted power function to Wei et al. (2017). This result is somewhat expected since LAI_{un} is an input to 3SEB. Nonetheless, it illustrates the advantage of decomposing the flux and vegetation components in TGEs. Indeed, this has important implications for land surface models, which often rely heavily on LAI through a 'big leaf' approach (e.g., Lian et al, 2018). While certain models consider horizontal heterogeneity within modeling grids, the integration of different vertical layers (e.g. overstory and understory) are rarely considered in Earth system models. As shown in Bonan et al. (2021), 'big leaf' canopies may oversimplify complex vertical vegetation structures and processes, resulting in poorer model robustness compared to multi-layered models. This canopy misrepresentation is particularly relevant in TGEs, having two vegetation layers with highly different survival strategies and characteristics, making it inadequate to relate singular bulk biophysical variables to represent vegetation functioning at the ecosystem scale (as supported by Fig. 11). The simple, yet effective, dual vegetation layer representation in 3SEB is a way forward for future model development, particular for landscapes with important differences in the overstory and understory canopies.

The 3SEB processed-based T/ET partitioning compared well with the data-driven TEA, even though they have very different and independent approaches. While T_{TEA} is not a measured dataset, its highly data-driven approach allows for an appropriate benchmark, especially considering the limitations (an unavailability) of T/ET measurements, such as sap flux or isotopic methods (Anderson et al., 2017; Kool et al., 2014). TEA exploits ET's link with GPP and does not incorporate inputs related to vegetation structure (e.g., h_c, LAI). Despite this, the sites assessed rendered high T correlations from both methods ($r > 0.75$) and obtained similar magnitudes. The largest discrepancies occurred in US-Ton during the summer drought, with large T_{3SEB} overestimations compared to T_{TEA}. The understory EC tower in US-Ton corroborated this pattern, as the model systematically overestimated H_{sub} (H_{un} + H_{soil}) (Fig. 8). Total ecosystem H was well modeled and even slightly underestimated (see Fig.S3), indicating that H_{ov} was substantially underestimated. Since the residual of the energy balance determined LE, the underestimated H_{ov} suggests LE_{ov} was overestimated, as supported through the T_{TEA} comparison.

The apparent LE_{ov} overestimation in US-Ton may be linked to the constant LAI_{ov} forced into 3SEB, including uncertainty in capturing US-Ton's more dynamic deciduous overstory phenology. This would primarily affect the amount of radiation intercepted (and available) by overstory (i.e. Rn_{ov}) as LAI is the main input of the RTM within 3SEB (section S1 in SI). However, the estimated leaf-on LAI_{ov} in US-Ton (and other sites) was well captured compared to previous measurements found in the literature (see S4.2 in SI). In fact, a local sensitivity analysis of LAI_{ov} showed very little effect of this input on T/ET estimates (Fig. S5). As shown in Ryu et al. (2012) with upward-point cameras in US-Ton, LAI_{ov} peaks during the initial leaf-on period at around ~0.85 m^2/m^2, but gradually declines to ~0.7 m^2/m^2, before the rapid decrease in LAI during the leaf-off. Additionally, during the same seasonal period, Xu and Baldocchi (2003) showed gradual decreases in carbon assimilation and stomatal conductance from the tree overstory. These results demonstrate their conservative water saving strategies during dry conditions. Similar observations were reported for trees in both Spanish and Australian sites (Luo et al., 2018; Moore et al., 2016)

These findings suggest that trees in semi-arid climates hold a strong physiological control on ET, regulating their stomata during periods of sustained increases in atmospheric vapour pressure deficit (VPD) (Niinemets, 2015; Pérez-Priego et al., 2010; Villalobos et al., 2012, 2000). 3SEB may not adequately depict this stomatal control, especially in relation to VPD, resulting in the LE_{ov} overestimation apparent in US-Ton. This effect is likely more pronounced in US-Ton, due to the larger tree overstory canopy cover (48%) compared to other sites (~20%). Certain studies suggested that the potential PT coefficient (i.e., α_{PT} in Eq. 5.1) is closer to ~1 in trees, even with ample water availability, instead of the widely used 1.26 (Andreu et al., 2018; Baldocchi and Xu, 2007; Black, 1979; Shuttleworth and Calder, 1979). To test this, 3SEB was also forced with $\alpha_{PT} = 1$ for the overstory ET initialization, which slightly improved T/ET estimates in US-Ton (Fig. S6) but further underestimated ET in AU-Dry (data not shown). This suggests that 3SEB should directly incorporate the physiological control of stomatal resistance, instead of calibrating the α_{PT} parameter. Colaizzi et al. (2014) applied the Penman-Monteith (PM) formulation within TSEB to derive the initial canopy T, which resulted in better T/ET agreement over a semi-arid cultivated site compared to the PT approach. However, they applied it with a constant maximum stomatal conductance. Therefore, the use of a tree stomatal closure constraint with increasing VPD (e.g., Damour et al., 2010; Miner et al., 2017), coupled with the PM initialization, may be a way forward to improve 3SEB's T_{ov}/ET estimates.

The proposed MODIS-based LAI partitioning method seemingly captured the understory LAI dynamics in both magnitude and timing for TGEs (Section S4.2 in SI). The retrieved LAI_{un} had low errors compared to *in-situ* destructive measurements in ES-LM1 and US-Ton (Fig. 4). However, ES-LM1 observed important LAI_{un} underestimations against LAI_{total}, especially during the dry periods of highly productive years. Very low LAI_{un} values (i.e., < 0.5 m^2/m^2) during the seasonal drought caused non-linear increases to the bulk vegetation resistance R_x (data not shown), which is negatively related to LAI (Eq. S11). These highly productive years led to increased amounts of remaining dry vegetation biomass during the seasonal drought period. The dead vegetation, while not active, increased the roughness of the landscape. This issue induced more aerodynamic conductivity and H. This situation was most evident during 'wet' years with large vegetation productivity, most visible in 2016 for ES-Abr and ES-LM1, which suffered important LE biases during the seasonal drought (Fig. 5). The *in-situ* data in ES-LM1 revealed that LAI_{total} remained between 0.5-1 m^2/m^2 during the peak drought period. By contrast, the MODIS estimated LAI_{un} was < 0.4 m^2/m^2. MODIS LAI product refers to LAI_{green} (Fensholt et al., 2004), whereas LAI_{total} affects the resistance and radiation partition of the landscape. This demonstrated the R_x sensitivity to the LAI uncertainty at very low magnitudes, which should include non-green elements (i.e., LAI_{total} or PAI). During the growing season, high LAI values are largely composed of green material, making LAI_{green} a good estimate of LAI_{total}. However, LAI_{total} deviated from LAI_{green} during the seasonal drought due to the large presence of senescent vegetation.

The effect of senescent vegetation on biophysical variables remains challenging to quantify (Martín et al. 2020; Melendo-Vega et al., 2018; Pacheco-Labrador et al., 2020). More specific retrieval methods, such as applying RTMs incorporating senescent vegetation may improve LAI estimations (e.g., SenSCOPE; Pacheco-Labrador et al., 2020; Proctor et al., 2017). The need for a complete annual time series, with both rainy and dry seasons, was another drawback of the LAI partitioning method presented here. This makes the current model set-up applicable for only non-time-critical diagnosis or hindcast purposes as it cannot dynamically separate LAI as it is prescribed. Spectral unmixing techniques (e.g., Meyer and Okin, 2015) may be a way forward to improve the LAI retrievals and partitioning in these dual-vegetated landscapes. Other data streams like spaceborne LiDAR data from NASA's GEDI mission also open new opportunities to retrieve more accurate plant structural (e.g., h_c, f_c) and biophysical (e.g., PAI) variables in complex ecosystems (Dubayah et al. 2020). Other remaining challenges include adequately quantifying the Rn in these heterogenous landscapes, particularly with the use of global shortwave irradiance inputs. The 3SEB estimated Rn remains slightly underestimated (see Table S2 in SI) with scarce measured data available to validate its decomposition across canopy sources. Three-dimensional RTMs, such as the Discrete Anisotropic Radiative Transfer (DART) model (Gastellu-Etchegorry et al., 2015) or as described by Kobayashi et al. (2012) may serve as a framework to better characterize Rn in these complex ecosystems.

5. Conclusions

The novel, yet structurally simple, 3SEB model offers new avenues to improve drought monitoring and investigate the different plant water uses in semi-arid TGEs. ET and energy flux retrievals over these complex, multi-layered ecosystems is a challenging and well-documented issue (Andreu et al. 2018; Burchard-Levine et al. 2020, Majozi et al. 2017; Ramoelo et al. 2014; Whitley et al. 2017), despite being critical for the global carbon and water cycle (Ahlström et al., 2015; Jung et al., 2011; Poulter et al., 2014).The dual vegetation strata, the grass dominated understory and tree dominated overstory, have distinct structural, physiological and phenological characteristics that should be considered within modeling schemes (Whitley et al. 2017). 3SEB accommodated an additional vegetation source to the well-known TSEB to accomplish this, improving their depiction and effect on energy fluxes.

The 3SEB model achieved accurate ET estimations during four-year periods over sites in Australia, Spain (2) and USA (ET RMSD: ~0.4 mm/day and NSE > 0.8). The model performed well despite the highly variable climatic and vegetation conditions. 3SEB largely improved the energy flux modeling compared to TSEB and TSEB-2S. It slightly underestimated ET for AU-Dry due to H overestimation during the peak biomass. By contrast, ES-LM1 and US-Ton slightly overestimated LE during the seasonal drought, particularly for highly productive (i.e., 'wet') years. This issue was linked to the R_x overestimation at very low LAI values (< 0.5 m^2/m^2). The LAI_{un} input was slightly underestimated compared to field measurements in ES-LM1 and US-Ton, and particularly lower compared to LAI_{total} measurements in ES-LM1. This highlights the importance of accounting for the large effect of senescent vegetation on remote sensing derived LAI products, notably in semi-arid ecosystems, which play an important role in the transfer of radiation and turbulence. Continental-scale 3SEB results forced with SEVIRI/MSG data also showed promising results. However, the larger uncertainty from model inputs, particularly shortwave irradiance, and spatial mismatch between pixel and tower scales caused larger modeling errors.

3SEB additionally separated ET into the different tree-grass-soil components of the landscapes, not previously possible with available data-driven methods. The 3SEB T/ET partitioning compared well to the data-driven TEA algorithm ($r > 0.76$) and demonstrated the contrasting relations of the two vegetation layers in TGEs with seasonal P. This fact confirmed their different survival strategies. T/ET was not very correlated with LAI_{MODIS} at the ecosystem level. However, the relation was much stronger when decomposing T/ET and LAI into the different vegetation layers. These findings should alleviate the disproportionally large uncertainty of global remote sensing-based ET products in these important and extensive ecosystems, along with offering a simple multi-layer approach of potential use to Earth system models. 3SEB presents a new framework to understand the role of complex and distinct vegetation dynamics, at both temporal and spatial scales, in modulating ecosystem level fluxes and water scarcity.

6. Acknowledgments

The research received funding from the European Union's Horizon 2020 research and innovation programme under the Marie Sklodowska-Curie TRuStEE project (grant agreement No 721995). It was also funded by Ministerio de Economía y Competitividad through SynerTGE CGL2015-G9095-R funded by MCIN/ AEI /10.13039/501100011033/ FEDER "a way of making Europe". The infrastructure at ES-LM1 was partly funded through the Alexander von Humboldt Foundation, ELEMENTAL (CGL 2017-83538-C3-3-R, MINECO-FEDER) and IMAGINA (PROMETEU 2019; Generalitat Valenciana). Funding for the US-Ton AmeriFlux site was provided by the U.S. Department of Energy's Office of Science. This research was also supported by the NASA Ecostress project. We thank Siyan Ma for contributing to the collection and processing of US-Ton's *in-situ* data.

Data Availability statement: The 3SEB model code is available through its public Github repository: https://github.com/VicenteBurchard/3SEB. Biometeorological data were collected for AU-Dry (Hutley et al., 2011) through the Ozflux portal: http://www.ozflux.org.au/monitoringsites/dryriver/; for US-Ton (Ma et al., 2021) through the Ameriflux portal: https://ameriflux.lbl.gov/sites/siteinfo/US-Ton; for ES-Abr (El-Madany et al., 2020) through its public repository: https://zenodo.org/record/3707842#.YWMEAtpByyz and for ES-LM1 (El-Madany et al., 2018; 2021) through its public repository: https://zenodo.org/record/4453567#.YWMEDNpByyw. In addition, to evaluate the continental scale evaluation, data for SN-Dhr (Tagesson et al., 2013; 2015; http://sites.fluxdata.org/SN-Dhr/) and ZA-Kru (Archibald et al., 2009; Scholes, 2013; http://sites.fluxdata.org/ZA-Kru/) were collected from the FLUXNET2015 release (Pastorello et al., 2020). MODIS LAI and NDVI data were collected through the ORNL DAAC subset and visualization tool: https://doi.org/10.3334/ORNLDAAC/1379. SEVIRI/MSG data were acquired from Land Surface Analysis Satellite Application Facilities (LSA SAF) (https://landsaf.ipma.pt/en/data/catalogue/). Please refer to section 8 of the Supplementary Information for links to these datasets.

7. References

Agam, N., Kustas, W.P., Anderson, M.C., Norman, J.M., Colaizzi, P.D., Howell, T.A., Prueger, J.H., Meyers, T.P., Wilson, T.B., 2010. Application of the Priestley–Taylor Approach in a Two-Source Surface Energy Balance Model. J. Hydrometeor. 11, 185–198.

Ahlström, A., Raupach, M.R., Schurgers, G., Smith, B., Arneth, A., Jung, M., Reichstein, M., Canadell, J.G., Friedlingstein, P., Jain, A.K., 2015. The dominant role of semi-arid ecosystems in the trend and variability of the land CO2 sink. Science 348, 895–899.

Allen, R.G., Tasumi, M., Trezza, R., 2007. Satellite-Based Energy Balance for Mapping Evapotranspiration with Internalized Calibration (METRIC)—Model. Journal of Irrigation and Drainage Engineering 133, 380–394.

Anderson, M.C., Norman, J.M., Diak, G.R., Kustas, W.P., Mecikalski, J.R., 1997. A two-source time-integrated model for estimating surface fluxes using thermal infrared remote sensing. Remote sensing of environment 60, 195–216.

Anderson, M.C., Yang, Yang, Xue, J., Knipper, K.R., Yang, Yun, Gao, F., Hain, C.R., Kustas, W.P., Cawse-Nicholson, K., Hulley, G., Fisher, J.B., Alfieri, J.G., Meyers, T.P., Prueger, J., Baldocchi, D.D., Rey-Sanchez, C., 2020. Interoperability of ECOSTRESS and Landsat for mapping evapotranspiration time series at sub-field scales. Remote Sensing of Environment 112189.

Anderson, R.G., Zhang, X., Skaggs, T.H., 2017. Measurement and Partitioning of Evapotranspiration for Application to Vadose Zone Studies. Vadose Zone Journal 16, vzj2017.08.0155.

Andreu, A., Kustas, W., Polo, M., Carrara, A., González-Dugo, M., 2018. Modeling Surface Energy Fluxes over a Dehesa (Oak Savanna) Ecosystem Using a Thermal Based Two Source Energy Balance Model (TSEB) II—Integration of Remote Sensing Medium and Low Spatial Resolution Satellite Images. Remote Sensing 10, 558.

Archibald, S., Scholes, R.J., 2007. Leaf green-up in a semi-arid African savanna-separating tree and grass responses to environmental cues. Journal of Vegetation Science 18, 583–594.

Baldocchi, D., Ma, S., 2013. How will land use affect air temperature in the surface boundary layer? Lessons learned from a comparative study on the energy balance of an oak savanna and annual grassland in California, USA. Tellus B: Chemical and Physical Meteorology 65, 19994.

Baldocchi, D.D., 2020. How eddy covariance flux measurements have contributed to our understanding of Global Change Biology. Global Change Biology 26, 242–260.

Baldocchi, D.D., Chen, Q., Chen, X., Ma, S., Miller, G., Ryu, Y., Xiao, J., Wenk, R., Battles, J., 2010. The dynamics of energy, water and carbon fluxes in a blue oak (Quercus douglasii) savanna in California, USA. Ecosystem Function in Global Savannas: Measurement and Modeling at Landscape to Global Scales 135–151.

Baldocchi, D.D., Xu, L., 2007. What limits evaporation from Mediterranean oak woodlands–The supply of moisture in the soil, physiological control by plants or the demand by the atmosphere? Advances in Water Resources 30, 2113–2122.

Bastiaanssen, W.G.M., 2000. SEBAL-based sensible and latent heat fluxes in the irrigated Gediz Basin, Turkey. Journal of hydrology 229, 87–100.

Biederman, J.A., Scott, R.L., Bell, T.W., Bowling, D.R., Dore, S., Garatuza-Payan, J., Kolb, T.E., Krishnan, P., Krofcheck, D.J., Litvak, M.E., Maurer, G.E., Meyers, T.P., Oechel, W.C., Papuga, S.A., Ponce-Campos, G.E., Rodriguez, J.C., Smith, W.K., Vargas, R., Watts, C.J., Yepez, E.A., Goulden, M.L., 2017. CO2 exchange and evapotranspiration across dryland ecosystems of southwestern North America. Global Change Biology 23, 4204–4221.

Black, T.A., 1979. Evapotranspiration from Douglas fir stands exposed to soil water deficits. Water Resources Research 15, 164–170.

Bonan, G. B., Patton, E. G., Finnigan, J. J., Baldocchi, D. D., & Harman, I. N. (2021). Moving beyond the incorrect but useful paradigm: Reevaluating big-leaf and multilayer plant canopies to model biosphere-atmosphere fluxes – a review. Agricultural and Forest Meteorology, 306, 108435.

Bogdanovich, E., Perez-Priego, O., El-Madany, T.S., Guderle, M., Pacheco-Labrador, J., Levick, S.R., Moreno, G., Carrara, A., Pilar Martín, M., Migliavacca, M., 2021. Using terrestrial laser scanning for characterizing tree structural parameters and their changes under different management in a Mediterranean open woodland. Forest Ecology and Management 486, 118945.

Bond, W.J., 2008. What Limits Trees in C4 Grasslands and Savannas? Annual Review of Ecology, Evolution, and Systematics 39, 641–659.

Bond, W.J., Midgley, G.F., Woodward, F.I., 2003. The importance of low atmospheric CO2 and fire in promoting the spread of grasslands and savannas. Global Change Biology 9, 973–982.

Boulet, G., Mougenot, B., Lhomme, J.-P., Fanise, P., Lili-Chabaane, Z., Olioso, A., Bahir, M., Rivalland, V., Jarlan, L., Merlin, O., Coudert, B., Er-Raki, S., Lagouarde, J.-P., 2015. The SPARSE model for the prediction of water stress and evapotranspiration components from thermal infra-red data and its evaluation over irrigated and rainfed wheat. Hydrology and Earth System Sciences 19, 4653–4672.

Burchard-Levine, V., Nieto, H., Riaño, D., Migliavacca, M., El-Madany, T.S., Perez-Priego, O., Carrara, A., Martín, M.P., 2020. Seasonal Adaptation of the Thermal-Based Two-Source Energy Balance Model for Estimating Evapotranspiration in a Semiarid Tree-Grass Ecosystem. Remote Sensing 12, 904.

Burchard-Levine, V., Nieto, H., Riaño, D., Migliavacca, M., El-Madany, T.S., Guzinski, R., Carrara, A., Martín, M.P., 2021. The effect of pixel heterogeneity for remote sensing based retrievals of evapotranspiration in a semi-arid tree-grass ecosystem. Remote Sensing of Environment 260, 112440.

Campbell, G.S., Norman, J.M., 1998. An Introduction to Environmental Biophysics, 2nd Edition. ed. Springer-Verlag New York, New York.

Casals, P., Gimeno, C., Carrara, A., Lopez-Sangil, L., Sanz, M., 2009. Soil CO2 efflux and extractable organic carbon fractions under simulated precipitation events in a Mediterranean Dehesa. Soil Biology and Biochemistry 41, 1915–1922.

Cawse-Nicholson, K., Braverman, A., Kang, E.L., Li, M., Johnson, M., Halverson, G., Anderson, M., Hain, C., Gunson, M., Hook, S., 2020. Sensitivity and uncertainty quantification for the ECOSTRESS evapotranspiration algorithm – DisALEXI. International Journal of Applied Earth Observation and Geoinformation 89, 102088.

Chu, H., Baldocchi, D.D., John, R., Wolf, S., Reichstein, M., 2017. Fluxes all of the time? A primer on the temporal representativeness of FLUXNET. Journal of Geophysical Research: Biogeosciences 122, 289–307.

Chu, H., Luo, X., Ouyang, Z., Chan, W. S., Dengel, S., Biraud, S. C., Torn, M. S., Metzger, S., Kumar, J., Arain, M. A., Arkebauer, T. J., Baldocchi, D., Bernacchi, C., Billesbach, D., Black, T. A., Blanken, P. D., Bohrer, G., Bracho, R., Brown, S., … Zona, D. (2021). Representativeness of Eddy-Covariance flux footprints for areas surrounding AmeriFlux sites. Agricultural and Forest Meteorology, 301–302, 108350.

Cleugh, H.A., Leuning, R., Mu, Q., Running, S.W., 2007. Regional evaporation estimates from flux tower and MODIS satellite data. Remote Sensing of Environment 106, 285–304.

Colaizzi, P.D., Agam, N., Tolk, J.A., Evett, S.R., Howell, T.A., Gowda, P.H., O'Shaughnessy, S.A., Kustas, W.P., Anderson, M.C., 2014. Two-source energy balance model to calculate E, T, and ET: Comparison of Priestley-Taylor and Penman-Monteith formulations and two time scaling methods. Transactions of the ASABE 57, 479–498.

Damour, G., Simonneau, T., Cochard, H., Urban, L., 2010. An overview of models of stomatal conductance at the leaf level. Plant, Cell & Environment 33, 1419–1438.

Deng, W., Bai, J., Yan, M., 2002. Problems and countermeasures of water resources for sustainable utilization in China. Chinese Geographical Science 12, 289–293.

Donohue, R.J., McVICAR, T.R., Roderick, M.L., 2009. Climate-related trends in Australian vegetation cover as inferred from satellite observations, 1981–2006. Global Change Biology 15, 1025–1039.

Dugas, W.A., Fritschen, L.J., Gay, L.W., Held, A.A., Matthias, A.D., Reicosky, D.C., Steduto, P., Steiner, J.L., 1991. Bowen ratio, eddy correlation, and portable chamber measurements of sensible and latent heat flux over irrigated spring wheat. Agricultural and Forest Meteorology 56, 1–20.

El-Madany, T.S., Carrara, A., Martín, M.P., Moreno, G., Kolle, O., Pacheco-Labrador, J., Weber, U., Wutzler, T., Reichstein, M., Migliavacca, M., 2020. Drought and heatwave impacts on semi-arid ecosystems' carbon fluxes along a precipitation gradient. Philosophical Transactions of the Royal Society B.

El-Madany, T.S., Reichstein, M., Perez-Priego, O., Carrara, A., Moreno, G., Pilar Martín, M., Pacheco-Labrador, J., Wohlfahrt, G., Nieto, H., Weber, U., Kolle, O., Luo, Y.-P., Carvalhais, N., Migliavacca, M., 2018. Drivers of spatio-temporal variability of carbon dioxide and energy fluxes in a Mediterranean savanna ecosystem. Agricultural and Forest Meteorology 262, 258–278.

Fatichi, S., Pappas, C., 2017. Constrained variability of modeled T:ET ratio across biomes. Geophysical Research Letters 44, 6795–6803.

Fensholt, R., Sandholt, I., Rasmussen, M.S., 2004. Evaluation of MODIS LAI, fAPAR and the relation between fAPAR and NDVI in a semi-arid environment using in situ measurements. Remote Sensing of Environment 91, 490–507.

Fisher, J.B., Lee, B., Purdy, A.J., Halverson, G.H., Dohlen, M.B., Cawse-Nicholson, K., Wang, A., Anderson, R.G., Aragon, B., Arain, M.A., Baldocchi, D.D., Baker, J.M., Barral, H., Bernacchi, C.J., Bernhofer, C., Biraud, S.C., Bohrer, G., Brunsell, N., Cappelaere, B., Castro-Contreras, S., Chun, J., Conrad, B.J., Cremonese, E., Demarty, J., Desai, A.R., Ligne, A.D., Foltýnová, L., Goulden, M.L., Griffis, T.J., Grünwald, T., Johnson, M.S., Kang, M., Kelbe, D., Kowalska, N., Lim, J.-H., Maïnassara, I., McCabe, M.F., Missik, J.E.C., Mohanty, B.P., Moore, C.E., Morillas, L., Morrison, R., Munger, J.W., Posse, G., Richardson, A.D., Russell, E.S., Ryu, Y., Sanchez-Azofeifa, A., Schmidt, M., Schwartz, E., Sharp, I., Šigut, L., Tang, Y., Hulley, G., Anderson, M., Hain, C., French, A., Wood, E., Hook, S., 2020. ECOSTRESS: NASA's Next Generation Mission to Measure Evapotranspiration From the International Space Station. Water Resources Research 56, e2019WR026058.

Fisher, J.B., Melton, F., Middleton, E., Hain, C., Anderson, M., Allen, R., McCabe, M.F., Hook, S., Baldocchi, D., Townsend, P.A., Kilic, A., Tu, K., Miralles, D.D., Perret, J., Lagouarde, J.-P., Waliser, D., Purdy, A.J., French, A., Schimel, D., Famiglietti, J.S., Stephens, G., Wood, E.F., 2017. The future of evapotranspiration: Global requirements for ecosystem functioning, carbon and climate feedbacks, agricultural management, and water resources. Water Resources Research 53, 2618–2626.

Foken, T., Aubinet, M., Finnigan, J.J., Leclerc, M.Y., Mauder, M., Paw U, K.T., 2011. Results of a panel discussion about the energy balance closure correction for trace gases. Bulletin of the American Meteorological Society 92, ES13–ES18.

Friedl, M.A., Sulla-Menashe, D., Tan, B., Schneider, A., Ramankutty, N., Sibley, A., Huang, X., 2010. MODIS Collection 5 global land cover: Algorithm refinements and characterization of new datasets. Remote sensing of Environment 114, 168–182.

Fuller, D.O., Prince, S.D., Astle, W.L., 1997. The influence of canopy strata on remotely sensed observations of savanna-woodlands. International Journal of Remote Sensing 18, 2985–3009.

García, M., Sandholt, I., Ceccato, P., Ridler, M., Mougin, E., Kergoat, L., Morillas, L., Timouk, F., Fensholt, R., Domingo, F., 2013. Actual evapotranspiration in drylands derived from in-situ and satellite data: Assessing biophysical constraints. Remote Sensing of Environment 131, 103–118.

Gastellu-Etchegorry, J.-P., Yin, T., Lauret, N., Cajgfinger, T., Gregoire, T., Grau, E., Feret, J.-B., Lopes, M., Guilleux, J., Dedieu, G., 2015. Discrete Anisotropic Radiative Transfer (DART 5) for modeling airborne and satellite spectroradiometer and LIDAR acquisitions of natural and urban landscapes. Remote Sensing 7, 1667–1701.

Glenn, E.P., Huete, A.R., Nagler, P.L., Hirschboeck, K.K., Brown, P., 2007. Integrating Remote Sensing and Ground Methods to Estimate Evapotranspiration. Critical Reviews in Plant Sciences 26, 139–168.

González-Dugo, M.P., Chen, X., Andreu, A., Carpintero, E., Gómez-Giraldez, P.J., Carrara, A., Su, Z., 2021. Long-term water stress and drought assessment of Mediterranean oak savanna vegetation using thermal remote sensing. Hydrology and Earth System Sciences 25, 755–768.

Gonzalez-Dugo, M.P., Neale, C.M.U., Mateos, L., Kustas, W.P., Prueger, J.H., Anderson, M.C., Li, F., 2009. A comparison of operational remote sensing-based models for estimating crop evapotranspiration. Agricultural and Forest Meteorology 149, 1843–1853.

Gutman, G., Ignatov, A., 1998. The derivation of the green vegetation fraction from NOAA/AVHRR data for use in numerical weather prediction models. International Journal of remote sensing 19, 1533–1543.

Guzinski, R., Nieto, H., Jensen, R., Mendiguren, G., 2014. Remotely sensed land-surface energy fluxes at sub-field scale in heterogeneous agricultural landscape and coniferous plantation. Biogeosciences 11, 5021–5046.

Guzinski, R., Nieto, H., Sandholt, I., Karamitilios, G., 2020. Modelling High-Resolution Actual Evapotranspiration through Sentinel-2 and Sentinel-3 Data Fusion. Remote Sensing 12, 1433.

Higgins, S.I., Delgado-Cartay, M.D., February, E.C., Combrink, H.J., 2011. Is there a temporal niche separation in the leaf phenology of savanna trees and grasses? Journal of Biogeography 38, 2165–2175.

Hutley, L.B., Beringer, J., Isaac, P.R., Hacker, J.M., Cernusak, L.A., 2011. A sub-continental scale living laboratory: Spatial patterns of savanna vegetation over a rainfall gradient in northern Australia. Agricultural and Forest Meteorology, Savanna Patterns of Energy and Carbon Integrated Across the Landscape (SPECIAL) 151, 1417–1428.

Jönsson, P., Eklundh, L., 2004. TIMESAT—a program for analyzing time-series of satellite sensor data. Computers & Geosciences 30, 833–845.

Jung, M., Reichstein, M., Margolis, H.A., Cescatti, A., Richardson, A.D., Arain, M.A., Arneth, A., Bernhofer, C., Bonal, D., Chen, J., 2011. Global patterns of land-atmosphere fluxes of carbon dioxide, latent heat, and sensible heat derived from eddy covariance, satellite, and meteorological observations. Journal of Geophysical Research: Biogeosciences 116.

Kobayashi, H., Baldocchi, D.D., Ryu, Y., Chen, Q., Ma, S., Osuna, J.L., Ustin, S.L., 2012. Modeling energy and carbon fluxes in a heterogeneous oak woodland: a three-dimensional approach. Agricultural and Forest Meteorology 152, 83–100.

Kondo, J., Ishida, S., 1997. Sensible Heat Flux from the Earth's Surface under Natural Convective Conditions. Journal of the Atmospheric Sciences 54, 498–509.

Kool, D., Agam, N., Lazarovitch, N., Heitman, J. L., Sauer, T. J., & Ben-Gal, A. (2014). A review of approaches for evapotranspiration partitioning. Agricultural and Forest Meteorology, 184, 56–70.

Kustas, W., Li, F., Jackson, T., Prueger, J., MacPherson, J., Wolde, M., 2004. Effects of remote sensing pixel resolution on modeled energy flux variability of croplands in Iowa. Remote sensing of Environment 92, 535–547.

Kustas, W.P., Alfieri, J.G., Anderson, M.C., Colaizzi, P.D., Prueger, J.H., Evett, S.R., Neale, C.M., French, A.N., Hipps, L.E., Chávez, J.L., 2012. Evaluating the two-source energy balance model using local thermal and surface flux observations in a strongly advective irrigated agricultural area. Advances in Water Resources 50, 120–133.

Kustas, W.P., Alfieri, J.G., Nieto, H., Wilson, T.G., Gao, F., Anderson, M.C., 2019. Utility of the two-source energy balance (TSEB) model in vine and interrow flux partitioning over the growing season. Irrig Sci 37, 375–388.

Kustas, W.P., Anderson, M.C., 2009. Advances in thermal infrared remote sensing for land surface modeling. Agricultural and Forest Meteorology 149, 2071–2081.

Kustas, W.P., Norman, J.M., 2000. Evaluating the Effects of Subpixel Heterogeneity on Pixel Average Fluxes. Remote Sensing of Environment 74, 327–342.

Kustas, W. P., Norman, J.M., 1999. Evaluation of soil and vegetation heat flux predictions using a simple two-source model with radiometric temperatures for partial canopy cover. Agricultural and Forest Meteorology 94, 13–29.

Kustas, William P, Norman, J.M., 1999. Reply to comments about the basic equations of dual-source vegetation-atmosphere transfer models. Agricultural and Forest Meteorology 4.

Leuning, R., van Gorsel, E., Massman, W.J., Isaac, P.R., 2012. Reflections on the surface energy imbalance problem. Agricultural and Forest Meteorology 156, 65–74.

Lhomme, J.-P., Montes, C., Jacob, F., Prévot, L., 2012. Evaporation from heterogeneous and sparse canopies: on the formulations related to multi-source representations. Boundary-layer meteorology 144, 243–262.

Lhomme, J.-P., Troufleau, D., Monteny, B., Chehbouni, A., Bauduin, S., 1997. Sensible heat flux and radiometric surface temperature over sparse Sahelian vegetation II. A model for the kB^{-1} parameter. Journal of Hydrology, HAPEX-Sahel 188–189, 839–854.

Li, X., Gentine, P., Lin, C., Zhou, S., Sun, Z., Zheng, Y., Liu, J., Zheng, C., 2019. A simple and objective method to partition evapotranspiration into transpiration and evaporation at eddy-covariance sites. Agricultural and Forest Meteorology 265, 171–182. https://doi.org/10.1016/j.agrformet.2018.11.017

Li, Y., Kustas, W.P., Huang, C., Nieto, H., Haghighi, E., Anderson, M.C., Domingo, F., Garcia, M., Scott, R.L., 2019. Evaluating Soil Resistance Formulations in Thermal-Based Two-Source Energy Balance (TSEB) Model: Implications for Heterogeneous Semiarid and Arid Regions. Water Resources Research 55, 1059–1078.

Lian, X., Piao, S., Huntingford, C., Li, Y., Zeng, Z., Wang, X., Ciais, P., McVicar, T. R., Peng, S., & Ottle, C. (2018). Partitioning global land evapotranspiration using CMIP5 models constrained by observations. Nature Climate Change, 8(7), 640.

Luo, Y., El-Madany, T., Filippa, G., Ma, X., Ahrens, B., Carrara, A., Gonzalez-Cascon, R., Cremonese, E., Galvagno, M., Hammer, T., 2018. Using Near-Infrared-Enabled Digital Repeat Photography to Track Structural and Physiological Phenology in Mediterranean Tree–Grass Ecosystems. Remote Sensing 10, 1293.

Ma, S., Xu, L., Verfaillie, J., Baldocchi, D. (2021), AmeriFlux BASE US-Ton Tonzi Ranch, Ver. 13-5, AmeriFlux AMP, (Dataset). https://doi.org/10.17190/AMF/1245971

Ma, S., Eichelmann, E., Wolf, S., Rey-Sanchez, C., & Baldocchi, D. D. (2020). Transpiration and evaporation in a Californian oak-grass savanna: Field measurements and partitioning model results. Agricultural and Forest Meteorology, 295, 108204.

Majozi, N.P., Mannaerts, C.M., Ramoelo, A., Mathieu, R., Mudau, A.E., Verhoef, W., 2017. An Intercomparison of Satellite-Based Daily Evapotranspiration Estimates under Different Eco-Climatic Regions in South Africa. Remote Sensing 9, 307.

Martín, M.P., Pacheco-Labrador, J., González-Cascón, R., Moreno, G., Migliavacca, M., García, M., Yebra, M., Riaño, D., 2020. Estimation of essential vegetation variables in a dehesa ecosystem using reflectance factors simulated at different phenological stages. Revista de Teledetección 0, 31–48.

McNaughton, K.G., Van Den Hurk, B.J.J.M., 1995. A "Lagrangian" revision of the resistors in the two-layer model for calculating the energy budget of a plant canopy. Boundary-Layer Meteorology 74, 261–288.

Melendo-Vega, J.R., Martín, M.P., Pacheco-Labrador, J., González-Cascón, R., Moreno, G., Pérez, F., Migliavacca, M., García, M., North, P., Riaño, D., 2018. Improving the performance of 3-D radiative transfer model FLIGHT to simulate optical properties of a tree-grass ecosystem. Remote Sensing 10, 2061.

Mendiguren, G., Pilar Martín, M., Nieto, H., Pacheco-Labrador, J., Jurdao, S., 2015. Seasonal variation in grass water content estimated from proximal sensing and MODIS time series in a Mediterranean Fluxnet site. Biogeosciences 12, 5523–5535.

Meyer, T., Okin, G.S., 2015. Evaluation of spectral unmixing techniques using MODIS in a structurally complex savanna environment for retrieval of green vegetation, nonphotosynthetic vegetation, and soil fractional cover. Remote Sensing of Environment 161, 122–130.

Miner, G.L., Bauerle, W.L., Baldocchi, D.D., 2017. Estimating the sensitivity of stomatal conductance to photosynthesis: a review. Plant, Cell & Environment 40, 1214–1238.

Moore, C.E., Beringer, J., Evans, B., Hutley, L.B., McHugh, I., Tapper, N.J., 2016. The contribution of trees and grasses to productivity of an Australian tropical savanna. Biogeosciences 13, 2387–2403.

Moran, M.S., Humes, K.S., Pinter Jr, P.J., 1997. The scaling characteristics of remotely-sensed variables for sparsely-vegetated heterogeneous landscapes. Journal of Hydrology 190, 337–362.

Moriasi, D.N., Arnold, J.G., Van Liew, M.W., Bingner, R.L., Harmel, R.D., Veith, T.L., 2007. Model evaluation guidelines for systematic quantification of accuracy in watershed simulations. Transactions of the ASABE 50, 885–900.

Nelson, J.A., Carvalhais, N., Cuntz, M., Delpierre, N., Knauer, J., Ogée, J., Migliavacca, M., Reichstein, M., Jung, M., 2018. Coupling Water and Carbon Fluxes to Constrain Estimates of Transpiration: The TEA Algorithm. Journal of Geophysical Research: Biogeosciences 123, 3617–3632.

Nelson, J.A., Pérez-Priego, O., Zhou, S., Poyatos, R., Zhang, Y., Blanken, P.D., Gimeno, T.E., Wohlfahrt, G., Desai, A.R., Gioli, B., Limousin, J.-M., Bonal, D., Paul-Limoges, E., Scott, R.L., Varlagin, A., Fuchs, K., Montagnani, L., Wolf, S., Delpierre, N., Berveiller, D., Gharun, M., Marchesini, L.B., Gianelle, D., Šigut, L., Mammarella, I., Siebicke, L., Black, T.A., Knohl, A., Hörtnagl, L., Magliulo, V., Besnard, S., Weber, U., Carvalhais, N., Migliavacca, M., Reichstein, M., Jung, M., 2020. Ecosystem transpiration and evaporation: Insights from three water flux partitioning methods across FLUXNET sites. Global Change Biology 26, 6916–6930.

Niinemets, Ü., 2015. Is there a species spectrum within the world-wide leaf economics spectrum? Major variations in leaf functional traits in the Mediterranean sclerophyll Quercus ilex. New Phytologist 205, 79–96.

Norman, J., Anderson, M., Kustas, W., French, A., Mecikalski, J., Torn, R., Diak, G., Schmugge, T., Tanner, B., 2003. Remote sensing of surface energy fluxes at 101-m pixel resolutions. Water Resources Research 39.

Norman, J.M., Kustas, W.P., Humes, K.S., 1995. Source approach for estimating soil and vegetation energy fluxes in observations of directional radiometric surface temperature. Agricultural and Forest Meteorology 77, 263–293.

ORNL DAAC. 2018. MODIS and VIIRS Land Products Global Subsetting and Visualization Tool. ORNL DAAC, Oak Ridge, Tennessee, USA. https://doi.org/10.3334/ORNLDAAC/1379

Pacheco-Labrador, J., El-Madany, T.S., Martín, M.P., Migliavacca, M., Rossini, M., Carrara, A., Zarco-Tejada, P.J., 2017. Spatio-Temporal Relationships between Optical Information and Carbon Fluxes in a Mediterranean Tree-Grass Ecosystem. Remote Sensing 9, 608.

Pacheco-Labrador, J., El-Madany, T.S., Tol, C. van der, Martín, M.P., Gonzalez-Cascon, R., Perez-Priego, O., Guan, J., Moreno, G., Carrara, A., Reichstein, M., Migliavacca, M., 2020. senSCOPE: Modeling radiative transfer and biochemical processes in mixed canopies combining green and senescent leaves with SCOPE. bioRxiv 2020.02.05.935064.

Perez-Priego, O., El-Madany, T.S., Migliavacca, M., Kowalski, A.S., Jung, M., Carrara, A., Kolle, O., Martín, M.P., Pacheco-Labrador, J., Moreno, G., 2017. Evaluation of eddy covariance latent heat fluxes with independent lysimeter and sapflow estimates in a Mediterranean savannah ecosystem. Agricultural and forest meteorology 236, 87–99.

Perez-Priego, O., Katul, G., Reichstein, M., El-Madany, T.S., Ahrens, B., Carrara, A., Scanlon, T.M., Migliavacca, M., 2018. Partitioning eddy covariance water flux components using physiological and micrometeorological approaches. Journal of Geophysical Research: Biogeosciences.

Pérez-Priego, O., Testi, L., Orgaz, F., Villalobos, F.J., 2010. A large closed canopy chamber for measuring CO2 and water vapour exchange of whole trees. Environmental and Experimental Botany 68, 131–138.

Piao, S., Ciais, P., Huang, Y., Shen, Z., Peng, S., Li, J., Zhou, L., Liu, H., Ma, Y., Ding, Y., 2010. The impacts of climate change on water resources and agriculture in China. Nature 467, 43–51.

Poulter, B., Frank, D., Ciais, P., Myneni, R.B., Andela, N., Bi, J., Broquet, G., Canadell, J.G., Chevallier, F., Liu, Y.Y., Running, S.W., Sitch, S., van der Werf, G.R., 2014. Contribution of semi-arid ecosystems to interannual variability of the global carbon cycle. Nature 509, 600–603.

Proctor, C., Lu, B., He, Y., 2017. Determining the absorption coefficients of decay pigments in decomposing monocots. Remote Sensing of Environment 199, 137–153.

Ramoelo, A., Majozi, N., Mathieu, R., Jovanovic, N., Nickless, A., Dzikiti, S., 2014. Validation of Global Evapotranspiration Product (MOD16) using Flux Tower Data in the African Savanna, South Africa. Remote Sensing 6, 7406–7423.

Raupach, M.R., 1994. Simplified expressions for vegetation roughness length and zero-plane displacement as functions of canopy height and area index. Boundary-Layer Meteorology 71, 211–216.

Running, S.W., Baldocchi, D.D., Turner, D.P., Gower, S.T., Bakwin, P.S., Hibbard, K.A., 1999. A global terrestrial monitoring network integrating tower fluxes, flask sampling, ecosystem modeling and EOS satellite data. Remote sensing of environment 70, 108–127.

Ryu, Y., Verfaillie, J., Macfarlane, C., Kobayashi, H., Sonnentag, O., Vargas, R., Ma, S., Baldocchi, D.D., 2012. Continuous observation of tree leaf area index at ecosystem scale using upward-pointing digital cameras. Remote Sensing of Environment 126, 116–125.

Sala, O.E., Chapin, F.S., Iii, Armesto, J.J., Berlow, E., Bloomfield, J., Dirzo, R., Huber-Sanwald, E., Huenneke, L.F., Jackson, R.B., Kinzig, A., Leemans, R., Lodge, D.M., Mooney, H.A., Oesterheld, M., Poff, N.L., Sykes, M.T., Walker, B.H., Walker, M., Wall, D.H., 2000. Global Biodiversity Scenarios for the Year 2100. Science 287, 1770–1774.

Santanello, J.A., Friedl, M.A., 2003. Diurnal Covariation in Soil Heat Flux and Net Radiation. Journal of Applied Meteorology 42, 851–862.

Sauer, T.J., Norman, J.M., 1995. Simulated canopy microclimate using estimated below-canopy soil surface transfer coefficients. Agricultural and forest meteorology 75, 135–160.

Schlesinger, W.H., Jasechko, S., 2014. Transpiration in the global water cycle. Agricultural and Forest Meteorology 189–190, 115–117.

Scholes, B., 2000-2013. FLUXNET2015 ZA-Kru Skukuza, Dataset. https://doi.org/10.18140/FLX/1440188

Scott, R.L., Biederman, J.A., 2017. Partitioning evapotranspiration using long-term carbon dioxide and water vapor fluxes. Geophysical Research Letters 44, 6833–6840.

Sea, W.B., Choler, P., Beringer, J., Weinmann, R.A., Hutley, L.B., Leuning, R., 2011. Documenting improvement in leaf area index estimates from MODIS using hemispherical photos for Australian savannas. Agricultural and Forest Meteorology, Savanna Patterns of Energy and Carbon Integrated Across the Landscape (SPECIAL) 151, 1453–1461.

Sheffield, J., Wood, E.F., 2008. Projected changes in drought occurrence under future global warming from multi-model, multi-scenario, IPCC AR4 simulations. Climate dynamics 31, 79–105.

Shuttleworth, W.J., Calder, I.R., 1979. Has the Priestley-Taylor Equation Any Relevance to Forest Evaporation? Journal of Applied Meteorology and Climatology 18, 639–646.

Stoy, P.C., El-Madany, T.S., Fisher, J.B., Gentine, P., Gerken, T., Good, S.P., Klosterhalfen, A., Liu, S., Miralles, D.G., Perez-Priego, O., Rigden, A.J., Skaggs, T.H., Wohlfahrt, G., Anderson, R.G., Coenders-Gerrits, A.M.J., Jung, M., Maes, W.H., Mammarella, I., Mauder, M., Migliavacca, M., Nelson, J.A., Poyatos, R., Reichstein, M., Scott, R.L., Wolf, S., 2019. Reviews and syntheses: Turning the challenges of partitioning ecosystem evaporation and transpiration into opportunities. Biogeosciences 16, 3747–3775.

Su, Z., 2002. The Surface Energy Balance System (SEBS) for estimation of turbulent heat fluxes. Hydrol. Earth Syst. Sci. 6, 85–100.

Sulla-Menashe, D., Gray, J. M., Abercrombie, S. P., & Friedl, M. A. (2019). Hierarchical mapping of annual global land cover 2001 to present: The MODIS Collection 6 Land Cover product. Remote Sensing of Environment, 222, 183–194.

Sun, X., Wilcox, B. P., & Zou, C. B. (2019). Evapotranspiration partitioning in dryland ecosystems: A global meta-analysis of in situ studies. Journal of Hydrology, 576, 123–136.

Tagesson, T., Ardö, J. and Fensholt. R., 2010-2013. FLUXNET2015 SN-Dhr Dahra, Dataset. https://doi.org/10.18140/FLX/1440246.

Tagesson, T., Fensholt, R., Guiro, I., Rasmussen, M.O., Huber, S., Mbow, C., Garcia, M., Horion, S., Sandholt, I., Holm-Rasmussen, B., Göttsche, F.M., Ridler, M.-E., Olén, N., Lundegard Olsen, J., Ehammer, A., Madsen, M., Olesen, F.S., Ardö, J., 2015. Ecosystem properties of semiarid savanna grassland in West Africa and its relationship with environmental variability. Global Change Biology 21, 250–264.

Timmermans, W.J., Kustas, W.P., Anderson, M.C., French, A.N., 2007. An intercomparison of the Surface Energy Balance Algorithm for Land (SEBAL) and the Two-Source Energy Balance (TSEB) modeling schemes. Remote Sensing of Environment 108, 369–384.

Verhoef, A., De Bruin, H., Van Den Hurk, B., 1997. Some practical notes on the parameter kB- 1 for sparse vegetation. Journal of Applied Meteorology 36, 560–572.

Villalobos, F.J., Orgaz, F., Testi, L., Fereres, E., 2000. Measurement and modeling of evapotranspiration of olive (Olea europaea L.) orchards. European Journal of Agronomy 13, 155–163.

Villalobos, F.J., Perez-Priego, O., Testi, L., Morales, A., Orgaz, F., 2012. Effects of water supply on carbon and water exchange of olive trees. European Journal of Agronomy 40, 1–7.

Wang, G., 2005. Agricultural drought in a future climate: results from 15 global climate models participating in the IPCC 4th assessment. Climate dynamics 25, 739–753.

Wang, L., Good, S.P., Caylor, K.K., 2014. Global synthesis of vegetation control on evapotranspiration partitioning. Geophysical Research Letters 41, 6753–6757.

Wei, Z., Yoshimura, K., Wang, L., Miralles, D.G., Jasechko, S., Lee, X., 2017. Revisiting the contribution of transpiration to global terrestrial evapotranspiration. Geophysical Research Letters 44, 2792–2801.

Whitley, R., Beringer, J., Hutley, L.B., Abramowitz, G., De Kauwe, M.G., Evans, B., Haverd, V., Li, L., Moore, C., Ryu, Y., Scheiter, S., Schymanski, S.J., Smith, B., Wang, Y.-P., Williams, M., Yu, Q., 2017. Challenges and opportunities in land surface modelling of savanna ecosystems. Biogeosciences 14, 4711–4732.

Wilson, K., Goldstein, A., Falge, E., Aubinet, M., Baldocchi, D., Berbigier, P., Bernhofer, C., Ceulemans, R., Dolman, H., Field, C., Grelle, A., Ibrom, A., Law, B.E., Kowalski, A., Meyers, T., Moncrieff, J., Monson, R., Oechel, W., Tenhunen, J., Valentini, R., Verma, S., 2002. Energy balance closure at FLUXNET sites. Agricultural and Forest Meteorology, FLUXNET 2000 Synthesis 113, 223–243.

Xu, L., Baldocchi, D.D., 2003. Seasonal trends in photosynthetic parameters and stomatal conductance of blue oak (Quercus douglasii) under prolonged summer drought and high temperature. Tree physiology 23, 865–877.

Zhuang, W., Shi, H., Ma, X., Cleverly, J., Beringer, J., Zhang, Y., He, J., Eamus, D., Yu, Q., 2020. Improving Estimation of Seasonal Evapotranspiration in Australian Tropical Savannas using a Flexible Drought Index. Agricultural and Forest Meteorology 295, 108203.